LITHOS 540–541 (2026) 108681

Contents lists available at ScienceDirect

LITHOS

journal homepage: www.elsevier.com/locate/lithos

Research Article

The Lar alkaline igneous complex: Age, mineralogy, chemistry, and isotopes of a potassic post-collisional event in the Eastern Iran Magmatic Belt (Sistan Suture Zone, East Iran)☆

M. Ghiotto [a], C. Natali [a,*], A. Rabiee [b], A. Bragagni [a,1], E. Braschi [c], R. Avanzinelli [a], M. Casalini [a], S. Ghafaribijar [d], M. Arvin [d], F. Rossetti [b], S. Conticelli [a,e]

[a] Dipartimento di Scienze della Terra, Università degli Studi di Firenze, Via Giorgio La Pira, 4, 50121 Florence, Italy
[b] Dipartimento di Scienze, Università degli Studi di RomaTre, Largo San Leonardo Murialdo, 1, 00146 Rome, Italy
[c] Consiglio Nazionale delle Ricerche, Istituto di Geoscienze e Georisorse, Sezione di Firenze, Via Giorgio La Pira, 4, 50121 Florence, Italy
[d] Department of Geology, Faculty of Sciences, University of Shahid Bahonar, Kerman, Iran
[e] Consiglio Nazionale delle Ricerche, Istituto di Geoingegneria e Geologia Ambientale, Area della Ricerca RM1, Strada Provinciale 35d, 9, 00010 Montelibretti (RM), Italy

ARTICLE INFO

Keywords:
Lar Igneous complex
Alkaline magmatism
Shoshonitic/ultrapotassic
Sistan Suture Zone

ABSTRACT

This study investigates the Cenozoic magma genesis in the East Iran Magmatic Belt through a detailed petrographic, geochemical, and radiometric analysis of igneous rocks from the Lar alkaline complex in the Sistan Suture Zone (East Iran). The Lar complex consists of intrusive and hypabyssal rocks showing shoshonitic to ultrapotassic affinities with variable degrees of silica saturation. The most alkaline silica-undersaturated lithotypes include lamprophyres, nepheline-syenites, and felsic dykes of phonolitic composition, whereas silica-saturated and over-saturated rocks are represented by syenites, trachytic dykes and monzonites. U-Pb and K-Ar geochronological constraints indicate that intrusive and hypabyssal igneous rocks of the Lar complex were generated in a time span of *ca.* 3 Ma in the Early Oligocene (from 32.5 ± 0.4 to 29.3 ± 0.6 Ma). Lamprophyres and nepheline-syenites show pseudoleucite textures due to subsolidus unmixing forming nepheline and K-feldspar intergrowths. Incompatible trace element patterns show geochemical features compatible with a subduction-related setting (*i.e.*, large ion lithophile elements -LILE- enrichments and high field strength elements -HFSE- depletions), with the alkaline potassic and silica-undersaturated rocks characterized by higher light/heavy rare earth elements (LREE/HREE) fractionation (La_N/Yb_N from 12 to 22) with respect to the silica-saturated and -oversaturated rocks (La_N/Yb_N from 10 to 12). The initial Sr-Nd-Pb isotopic composition of the Lar igneous rocks is rather homogeneous ($^{87}Sr/^{86}Sr_i$ = 0.704295–0.706222, $^{143}Nd/^{144}Nd_i$ = 0.512627–0.512748, $^{206}Pb/^{204}Pb_i$ = 18.82–18.90, $^{207}Pb/^{204}$ Pb_i = 15.62–15.65, $^{208}Pb/^{204}Pb_i$ = 39.00–39.16) suggesting a common mantle source and limited crustal contamination/assimilation, which only affects the most differentiated products. The geochemical and isotopic features of the Lar magmas suggest that mantle metasomatism occurred as partial melts derived mainly from carbonate-rich sediments. The formation of the Lar igneous complex is attributed to post-collisional magmatism. This magmatism was triggered by asthenospheric upwelling that caused melting within the overlying mantle. Crucially, the mantle composition had been modified (metasomatized) by materials derived from the subducted Sistan Neo-Tethyan oceanic slab.

1. Introduction

Alkaline igneous rocks are found in different tectonic settings on Earth, both in intraplate settings, continental and oceanic, and at destructive plate margins. They are generated by partial melting of a variable metasomatized upper mantle (Edgar, 1987; Foley, 1992a). In

☆ This article is part of a Special issue entitled: 'Steve Foley Special Issue' published in LITHOS.

* Corresponding author at: Dipartimento di Scienze della Terra, Università degli Studi di Firenze, Via Giorgio La Pira, 4, 50121 Florence, Italy.
E-mail address: claudio.natali@unifi.it (C. Natali).
[1] Present address: Consiglio Nazionale delle Ricerche, Istituto di Scienze Marine, Via Gobetti 101, 40129, Bologna, Italy.

https://doi.org/10.1016/j.lithos.2026.108681
Received 24 December 2025; Received in revised form 8 June 2026; Accepted 13 June 2026
Available online 21 June 2026

the case of destructive plate margin setting metasomatism of the mantle wedge is originated by melts/fluids released by the subducted plate (*e.g.*, Avanzinelli et al., 2009; Elliott, 2003). The reaction between these agents and the peridotite of the mantle wedge creates metasomatic mantle domains characterized by the presence of amphibole and/or phlogopite, the main hydrated phases responsible for the generation of potassium-rich magmas (*e.g.*, Beccaluva et al., 2004; Bianchini et al., 2011; Conticelli et al., 2010, 2015; Foley, 1992a, 1992b).

The main Mesozoic and Cenozoic orogenic alkaline igneous complexes of the Iran region crop out to the west in the Zagros Mountains, along the Urumieh Dokhtar Magmatic Belt and the Sanandaj-Sirian Zone to the north in the Kopeh Dagh-Alborz Mountains, to the east along the East Iranian Magmatic Belt, and to the south in the Makran area (Dilek et al., 2010 and references therein; Fig. 1). The alkaline magmatism generally post-dated the main subduction-related calc-alkaline magmatism in the transition from oceanic subduction of the Neo-Tethyan oceanic branches to continental collision along the Alpine-Himalayan convergence zone (*e.g.*, Agard et al., 2011) especially prominent in the Eocene "flare-up" of the Urumieh Dokhtar Magmatic Belt (Agard et al., 2011; Pang et al., 2013; Verdel et al., 2011). Therefore, the study of these igneous occurrences is of the greatest importance for the geodynamic reconstruction of the closure of the Tethyan oceanic realm and the understanding of the P-T-X conditions involved in magma genesis in collisional to post-collisional environments.

In eastern Iran, orogenic suturing along the Sistan Suture Zone (SSZ) spanned from Late Cretaceous (Bonnet et al., 2018) to late Paleocene (Delavari et al., 2014), and middle-late Eocene (Mohammadi et al., 2023). The consequent lithospheric thickening led to the emplacement of ~86–71 Ma adakitic granodiorites and ~ 55 Ma A-type granites within the SSZ, commonly referred to as the partial melting of the thickened lower crust (U-Pb zircon dating; Zarrinkoub et al., 2012 and references therein). Cenozoic magmatism along the SSZ occurred in two main stages. The first stage occurred during the magmatic flare-up from middle-late Eocene to late Oligocene and led to the emplacement of calc-alkaline, high-K calc-alkaline and minor shoshonitic products along the SSZ (*e.g.*, Arjmandzadeh et al., 2011b; Arjmandzadeh and Santos, 2014; Mohammadi et al., 2016; Pang et al., 2013; Rabiee et al., 2022; Sargazi et al., 2022). The second stage, Late Miocene-Pliocene in age, was characterized by the eruption of intraplate ultrapotassic, adakitic, and alkali basalts, commonly emplaced along major strike-slip faults (Pang et al., 2013). The Cenozoic magmatism of the East Iranian Magmatic Belt is the results of a complex geodynamic evolution that has been variously attributed to slab rollback in an extensional regime (Verdel et al., 2011), post-collisional processes following the Lut–Afghan block

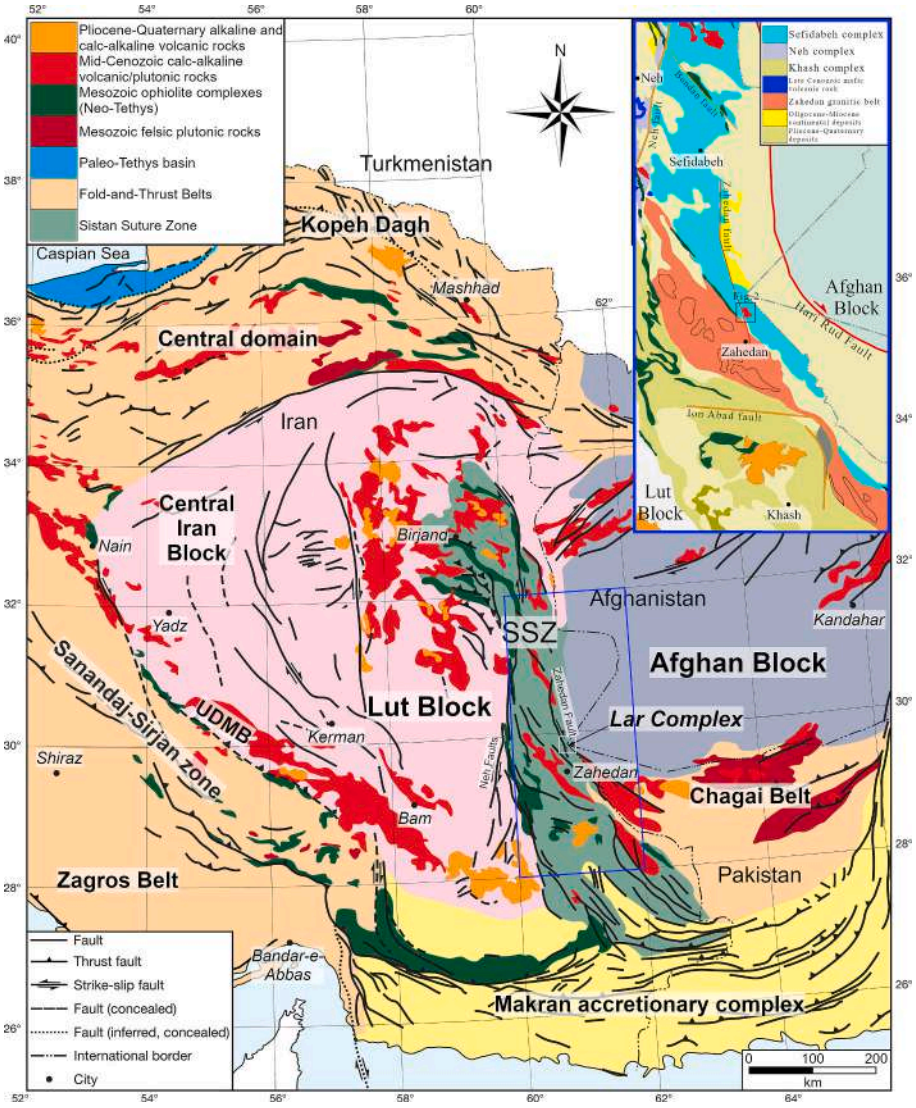

Fig. 1. Geology map of Mesozoic-Cenozoic igneous rocks and ophiolites of Iran, western Afghanistan, and western Pakistan, highlighting the Sistan Suture Zone (SSZ) and the location of the Lar Complex (modified from Richards et al., 2012 and references therein).

collision (*e.g.,* Omidianfar et al., 2020, 2023; Pang et al., 2013; Sepidbar et al., 2018), or an Andean-type subduction setting related to the closure of the Sistan Ocean (*e.g.,* Arjmandzadeh et al., 2011a; Nadermezerji et al., 2018; Samiee et al., 2016). Among the alkaline igneous complexes of the SSZ, the Oligocene Lar complex shows the widest variability of magmatic products including intrusive (syenites, monzonites), hypabyssal (lamprophyres, felsic dykes), and effusive (basalts, andesites, latites, trachites, leucitites, dacites and pyroclastic products) rocks (*e.g.,* Boomeri et al., 2019, 2020; Camp and Griffis, 1982; Ghafaribijar et al., 2019; Sargazi et al., 2022). Geological, geochemical and petrographic knowledge of the Lar complex is, to date, still very poor, despite its potential as Cu, Mo, and Au ore resource (Boomeri et al., 2019 and references therein).

This study reports a detailed investigation of intrusive and hypabyssal rocks (syenites, monzonites, lamprophyres and felsic dykes) of the Lar igneous complex with the aim of providing new insights on the age, nature, and evolution of the post-collisional magmatism of the SSZ. To achieve these goals, an integrated petrological approach was employed, combining petrographic investigations, bulk-rock major and trace element geochemical analyses, K-Ar whole rock and U-Pb zircon and apatite geochronology, and Sr–Nd–Pb isotopic systematics. Results are used to identify the magmatic affinities, the magma sources and the partial melting conditions. These characteristics are discussed in the framework of the geodynamic evolution of this sector of the Alpine-Himalayan belt.

2. Geological setting

The Iran region is an integral part of the Alpine–Himalayan orogenic system. It represents a tectonic collage of Gondwana-derived terranes that progressively accreted to the active southern margin of Eurasia during the consumption of the Paleo- and Neo-Tethyan oceanic branches (Agard et al., 2011; Berberian and King, 1981; Besse et al., 1998; Golonka, 2004; Rossetti et al., 2017; Stampfli et al., 2013; Zanchi et al., 2006; Zanchi et al., 2009). The terrane collision resulted in the development of distributed mountain belts during polyphase tectonic collision.

The SSZ is part of the Eastern Iranian Orogen (Bagheri and Damani Gol, 2020), extending for approximately 900 km in length and 200 km in width in the N-S direction along the present-day border of Iran, Pakistan, and Afghanistan. It formed by the closure of a Cretaceous (zircon U-Pb ages from gabbros ranging 113–104 Ma; Zarrinkoub et al., 2012; Bröcker et al., 2022 and references therein) oceanic branch of the Neo-Tethys (Sistan ocean), formerly located between the Lut Block (part of the Central Iran) to the west and the Afghan microcontinents to the east (Camp and Griffis, 1982; Tirrul et al., 1983; Fig.1). The geodynamic scenario and timing of the Cretaceous subduction of the Sistan Ocean remain subjects of debate. Current research generally proposes three main slab configurations: (i) northeastward directed intra-oceanic subduction (Saccani et al., 2010); (ii) subduction shift from southwestward- (Berberian and King, 1981; Pang et al., 2013; Zarrinkoub et al., 2012) to northeastward-directed during the Campanian (Camp and Griffis, 1982; Jentzer et al., 2022; Tirrul et al., 1983); and (iii) contemporaneous double-sided subduction during the Late Cretaceous (Arjmandzadeh et al., 2011a).

According to previous studies (Camp and Griffis, 1982; Ghasemi et al., 2010; Mohammadi et al., 2016; Moradi et al., 2014; Sadeghian and Valizadeh, 2007) the SSZ is composed of three main groups of rocks, named as the Neh, the Ratuk, and the Sefidabeh complexes, respectively, separated from each other by major N-S striking fault systems (inset of Fig. 1; Camp and Griffis, 1982; Tirrul et al., 1983; Bonnet et al., 2018; Bagheri and Damani Gol, 2020). The Neh geologic complex consists of a fold-and-thrust chain, formed by ophiolitic *mélanges*, shallow sea limestones, late Cretaceous-Oligocene deep-sea turbidites deposits (several hundred meters thick with Bouma sequences), and low-grade metamorphic rocks (*e.g.*, Carter et al., 2010; Mohammadi et al., 2016), which represent the outer portion of the accretionary prism formed during oceanic subduction (Tirrul et al., 1983). The Ratuk complex is also described as a pre-Maastrichtian accretionary prism. It includes Cretaceous ophiolitic *mélanges* and high-pressure (HP), subduction-related metamorphic rocks (eclogites, blueschists, and epidote amphibolites) dated about 81–87 Ma (zircon U-Pb, Rb-Sr and Ar-Ar dating; Bröcker et al., 2022; Kurzawa et al., 2017, Bonnet et al., 2018), lower Cretaceous limestones, late-Cretaceous turbidites, Eocene nummulitic limestones and Neogene conglomerates (*e.g.*, Delavari et al., 2014; Mohammadi et al., 2016; Tirrul et al., 1983). The Sefidabeh complex (including the Lar) rests unconformably upon the two underlying complexes, interpreted as a piggy-back forearc basin that developed atop the accretionary prism in the time preceding the Oligocene–Miocene (Tirrul et al., 1983; Mohammadi et al., 2016). It is formed by an association of clastic and volcanoclastic sediments with interposed low and deep-sea limestones and calc-alkaline magmatic rocks (Camp and Griffis, 1982; Mohammadi et al., 2016; Tirrul et al., 1983).

As reported by Moradi et al. (2016) and Boomeri et al. (2020) the igneous rocks from the SSZ have different petrologic affinities and ages, reflecting the various phases of the closure of the oceanic basin. Namely, they can be distinguished as follows: (i) late Cretaceous-Paleocene-Eocene subduction-related calc-alkaline volcanic rocks in the accretionary prism (*e.g.*, Camp and Griffis, 1982; Delavari et al., 2014; Tirrul et al., 1983); (ii) middle Eocene–early Oligocene calc-alkaline intrusive rocks (*i.e.,* granites – granodiorites – quartz-monzonites; *e.g.*, McCall, 1997; Camp and Griffis, 1982; Sadeghian and Valizadeh, 2007; Ghasemi et al., 2010; Moradi et al., 2014; Mohammadi et al., 2016); and (iii) Oligocene–middle Miocene calc-alkaline (shoshonitic) to alkaline volcanic rocks, related to the major post-collisional transcurrent tectonics (Camp and Griffis, 1982). Miocene-Quaternary alkaline and high potassium (HK) calc-alkaline magmatism are also present in the SSZ and occurs along the main strike-slip fault zones, characterizing the post-collisional phase (Pang et al., 2013).

2.1. The Lar Igneous complex

The Lar Igneous Complex is located about 20 km north of the city of Zahedan, in the southeastern Iran, along the mid-eastern side of the SSZ, near the Afghan block and belongs to the terranes of the Sefidabeh geologic complex (Fig. 1). According to previous studies, it is defined as a 9 × 4 km ellipse-shaped complex (Fig. 2) at the tip of the Zahedan fault (Boomeri et al., 2020). The Lar Igneous Complex is hosted within Late Cretaceous-Paleocene flyschoid rocks, composed by siliceous shales, sandstones, siltstones, and minor limestones, belonging to the Sefidabeh geologic complex (Figs. 1 and Fig. 2). The complex is composed of intrusive, hypabyssal, and volcanic rocks. Volcanic rocks are found in the central portion of the complex (Fig. 2) as lavas and pyroclastic rocks, ranging in composition from basalt, through andesite, to dacite, and from latite to trachite (*i.e.*, Boomeri et al., 2020). Leucitites are also reported among the volcanic rocks (*i.e.*, Boomeri et al., 2020). The hypabyssal rocks include felsic (*e.g.*, trachyte, phonolite, and syenite) and lamprophyric (*e.g.*, minette, spessartite, and vogesite) dykes (Fig. 2; *e.g.*, Boomeri et al., 2019, 2020; Ghafaribijar et al., 2019; Sargazi et al., 2022). The intrusive rocks primarily consist of monzonite, monzosyenite, syenite, large-perthitic nepheline syenite, and minor nepheline-bearing alkali feldspar syenite, and shonkinite. Available K-Ar ages for the intrusive lithologies of the Lar Igneous Complex are 32.8 ± 3 Ma (whole rock), 32.0 ± 1.6 Ma (whole rock) and 27.8 ± 3 Ma (biotite) (Camp and Griffis, 1982). Zircon U-Pb ages of 31.4 ± 0.3 and 31.6 ± 0.4 Ma derived from monzonite and monzosyenite, respectively, were recently reported by Sargazi et al. (2022).

The Lar Igneous Complex is characterized by hypogene and supergene alteration on its western and southwestern sides. Hypogene alteration is associated with Cu-Mo mineralization (chalcopyrite, bornite, molybdenite), whilst the supergene alteration is characterized by iron

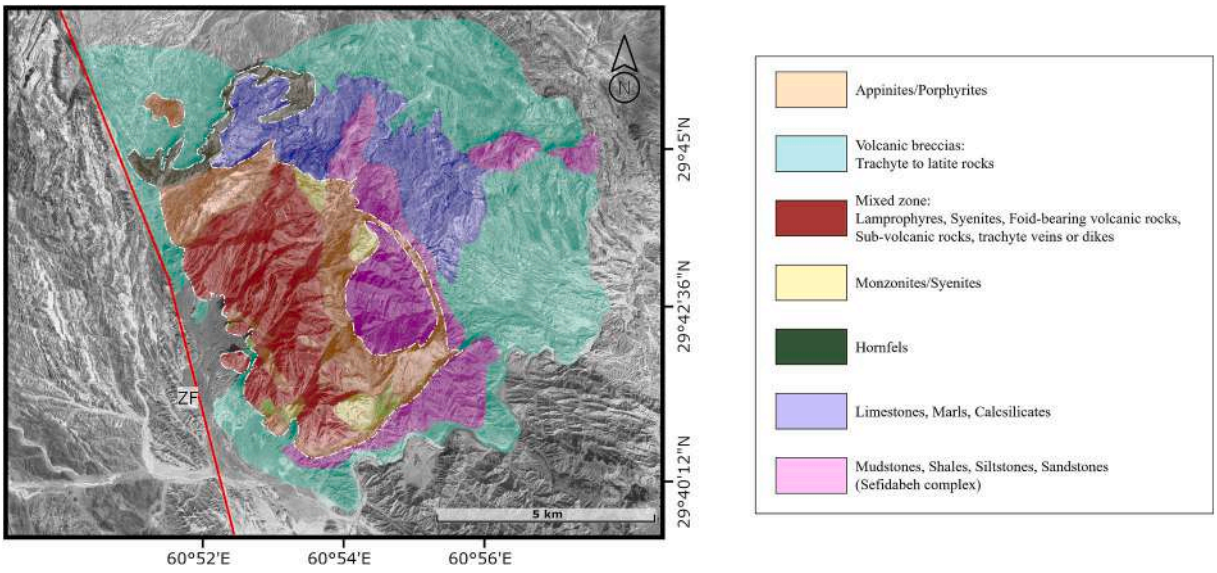

Fig. 2. Geology map of the Lar Complex (from Sargazi et al., 2022).

hydroxides, copper carbonates, chalcocite, native copper, enargite, limonite, malachite and azurite. The alteration is pervasive and is often associated with fractured areas (Boomeri et al., 2019). The contact with sedimentary rocks produced thermal metamorphism forming cornubianites and skarn-like rocks (grouped as hornfels in Fig. 2). The age of the mineralization event was dated between 31.95 ± 0.11 Ma and 29.72 ± 0.11 Ma based on *Re*-Os dating on molybdenites, providing a minimum age of 32 Ma for the magmatic event (Boomeri et al., 2019).

3. Materials and methods

The investigated samples include 33 intrusive and hypabyssal rocks representative of the lithologies of the peripheral zones of the Lar Igneous Complex.

Samples were cut using a diamond saw to isolate fresh cores free of superficial alteration. Each sample was split in two blocks, one was used to produce the thin section, whilst the other was crushed, quartered and powdered in an agate mill for dating, chemical and isotope analyses.

Petrographic observations were carried out on thin sections using a ZEISS AXIOSCOP polarized transmitted light microscope at the Department of Earth Sciences of the University of Florence (Italy).

Major and trace elements analyses on whole rock powders were performed by Activation Laboratories Ltd. (ActLabs; Ontario, Canada) following lithium metaborate digestion and ICP-OES and ICP-MS determination, respectively. Precision and accuracy were estimated to be better than 2% for SiO_2, Al_2O_3, Fe_2O_3 and MgO and better than 5% for the other major elements. Precision and accuracy of trace element analyses were within 10% (further analytical details can be found on the website www.actlabs.com). The analytical data are presented in the Supplementary Material (Table S1).

The Sr, Nd and Pb whole-rock isotopic analyses were performed at the Department of Earth Sciences of the University of Florence on 11 samples representative of the various rock suites. About 50 mg of sample powder was leached using 1 N HCl before digesting the samples in HF-HNO_3, details on the procedure are reported in Avanzinelli et al. (2005 and reference therein). Briefly, Sr and Pb purification was achieved by extraction ion chromatography using 140 µl pure quartz micro- filled with Sr-Resin (100–150 µm, Eichrom®). The matrix was eluted with 2 N HNO_3, before collecting Sr in Milli-Q® water and Pb in 6 N HCl. The evaporated matrix was redissolved in HCl 2.5 N and loaded in quartz column filled with AG50Wx8 cation exchange resin (200–400 mesh, Bio-Rad®). Rare Earth Elements (REE) were collected with 6 N HCl, after eluting the matrix in 2.5 N HCl. Then the REE fraction was loaded onto pure quartz column packed with pre-cleaned 2 ml Ln-Resin (100–150 µm, Eichrom®) and the final Nd fraction was eluted in 0.3 N HCl. The Sr, Nd, Pb isotope measurements were performed on a ThermoFisher Triton plus. Mass fractionation of Sr and Nd isotopes has been exponentially corrected with $^{86}Sr/^{88}Sr = 0.1194$ and $^{146}Nd/^{144}Nd = 0.7219$, respectively. The mass discrimination for Pb isotope measurements was determined by replicate analyses of the NIST SRM 981, and then applied to the unknown samples. Accuracy of the measurements was further tested through the measurements of international certified reference material AGV 1 yielding $^{87}Sr/^{86}Sr$ a = 0.703989 ± 0.000006 (2 s.e.), $^{143}Nd/^{144}Nd = 0.512776 \pm 0.000004$, $^{206}Pb/^{204}Pb = 18.945 \pm 0.006$, $^{207}Pb/^{204}Pb = 15.661 \pm 0.007$ and $^{208}Pb/^{204}Pb = 38.578 \pm 0.023$; all the isotopic ratios are identical, within error to reference values (Weis et al., 2006).

Back-scattered electron microscopy (BSEM) was used to map thin sections for apatite grains in lamprophyre (samples LL-52A and LL-62), Ne-syenite (sample LS29) and for zircon grains in lamprophyre, trachyte, monzonite, and phonolite (samples LL-62, LL-52B, LM-11, and LD-3, respectively). BSEM analyses were performed at the University of Florence - Interdepartmental Centre for Electron Microscopy and Microanalyses (MEMA)- using a Zeiss EVO MA15 SEM equipped with an Oxford EDS spectrometer. BSEM images of zircon and apatite grains are reported in Fig. S1.

In-situ U-Pb zircon and apatite dating was performed using LA-ICP-MS technique at the Department of Science, Roma Tre University. The LA-ICP-MS facility consists of a Teledyne Photon Machine Analyte Excite + ArF (193 nm) excimer laser ablation system coupled to a Thermo-Scientific, single quadrupole iCAP RQ spectrometer. The instrumental conditions were tuned to maximise the U signal at low oxide rates of <0.5% ($^{232}Th{\cdot}^{16}O/^{232}Th$). Laser spots size was set at 50 µm and 25 µm for apatite and zircon grains, respectively (for standards and unknown samples), with a 6 Hz, and ~ 4.0 J/cm^2 energy density. The ablation time was set at 65 s, comprising a background acquisition lasting 15 s, succeeded by a sample ablation period of 25 s, and followed by a 25 s washout phase. The measured masses include ^{29}Si, ^{31}P, ^{44}Ca, ^{90}Zr, ^{206}Pb, ^{207}Pb, ^{208}Pb, ^{232}Th, ^{238}U. The dwell times (ms) for the first four masses are 3 ms, and the rest are set to 45 ms. Further details regarding the instrumentation are provided in Rabiee et al. (2024). The zircon standard 91,500 (1065.4 ± 0.5 Ma; Wiedenbeck et al., 1995) was used for calibration and correction regarding the downhole mass fractionation effect, and three zircon standards, Plešovice (337.13 ± 0.37

Ma; Sláma et al., 2008), and OD-3 (33.0 ± 0.1 Ma, Iwano et al., 2013) were used for quality control, bracketing the unknown samples (8–10 unknown spots). The McClure Mountain Apatite (523.98 ± 0.12 Ma; Schoene and Bowring, 2006) was used as primary standard, while Durango apatite (31.44 ± 0.18 Ma; Chew et al., 2014) was used as secondary standard bracketing the unknown samples (8–10 unknown spots). Data reduction and corresponding corrections were performed through the Iolite_4 software (Paton et al., 2011). The U-Pb isotopic ratios for the zircons were calculated using U-Pb_Geochronology scheme, while for the apatites the VisualAge UcomPbine DRS module was utilized as described by Petrus and Kamber (2012) and Chew et al. (2014). The "live Concordia" tool in VisualAge module was utilized to select the best intervals for the spot signals, avoiding any surface- or inclusion-related contaminations. U-Pb age diagrams were plotted using IsoplotR toolbox (online version; Vermeesch, 2018). Due to the presence of variable common-Pb component in apatite and zircon grains, isotopic data are plotted on a Tera-Wasserburg diagram for Discordia age calculations (Ludwig, 2012). All reported uncertainties are at the 2σ level. Analytical results for zircon and apatite grains are shown in Supplementary Material as Table S2 and Table S3, respectively.

In situ U-Pb geochronology was complemented with whole rock K-Ar dating, performed by Activation Laboratories Ltd. (ActLabs, Ontario, Canada). An aliquot of the sample was weighted, loaded into the sample system of extraction unit and degassed at ca 100 °C for 2 days to remove the surface gases. Argon was extracted from the sample in double vacuum furnace at 1700 °C and its concentration determined using isotopic dilution with ^{38}Ar spike, which is introduced to the sample system prior to each extraction. The extracted gases are cleaned up in two-step purification system. Then, pure Ar is introduced into magnetic sector mass spectrometer (Reynolds type). Ar isotopic ratios were corrected for mass-discrimination and then atmospheric argon was removed assuming that ^{36}Ar is only from the air. Concentration of radiogenic ^{40}Ar was calculated by using ^{38}Ar spike concentration. K analysis was performed by ICP-OES.

4. Results

4.1. Petrography

The petrographic, modal and mineralogic features of the Lar Igneous Complex samples allowed their division into subvolcanic mafic (lamprophyres) and felsic (trachytic and phonolitic) dykes, whereas intrusive rocks were further divided into monzonite, syenite and nepheline-syenite. A summary of the mineralogical paragenesis of each sample is reported in Table 1.

4.1.1. Subvolcanic hypabyssal rocks

4.1.1.1. Lamprophyres. Lamprophyres show phaneritic highly porphyritic textures dominated by large (up to 1 cm) pale green clinopyroxene macrocrysts and phlogopite phenocrysts with minor olivine (Fig. 3a). K-feldspar, plagioclase (sometimes absent), with perthitic and antiperthitic features, and minor nepheline are interstitial late mineral phases. Following the mineralogical classification of Woolley et al. (1996), they can be classified as minette and kersantite, based on the relative abundance of alkali feldspar and plagioclase, respectively. No spessartite and vogesite dykes are recognized. Olivine is variably affected by isomorphic substitution of serpentine and sometimes preserving inner unaltered portions. Clinopyroxene also shows disequilibrium features such as corroded edges, and it is characterized by abundant phlogopite inclusions. The occurrence of phlogopite (Fig. 3b) both disseminated and included in clinopyroxene suggests that it persisted on the liquidus from the early crystallization stages. Abundant euhedral crystals of apatite (up to 0.7 mm) occur mainly as inclusions. Accessory minerals include magnetite, epidote and rutile. Phlogopite and feldspar are often partially replaced by chlorite and sericite, respectively. Some samples are characterized by the presence of ultramafic microenclaves (up to 4 mm), made up of clinopyroxene and minor oxides microcrystals and rimmed by phlogopite. Two samples (LL-31 and LL-55) are characterized by large (up to 2–3 cm) anhedral poikilitic alkali feldspars and by reaction borders on clinopyroxene and olivine crystals made of clay minerals. In these samples the presence of primary phlogopite is scarce, mainly in the form of reaction corona around magnetite, and partially replaced by chlorite (Fig. 3c). Pseudo-leucite textures, characterized by an intergrowth of anhedral nepheline and k-feldspar are observed, and plausibly originated by the leucite breakdown in intrusive conditions.

Table 1
Petrography of representative samples of Oliogcene igneous rocks from the Lar Camplex. Rock type, lithology, and affinity (SiO_2-undersaturated, SiO_2-oversaturated, and SiO_2saturated) are also reported. Cpx = clinopyroxene; kfs = k-feldspar; phl = phlogopite; ol = olivine; plg = plagioclase; ne = nepheline; qz = quartz; hbl = horneblende ap = apatite; ttn = titanite mag = magnetite; ilm = ilmenite; ep = epidote; rt. = rutile; zrn = zircon; zrc = zirconolite; thr = thorite; rbk = riebeckite; sid = siderophyllite.

Sample	Rock type	Lithology	Affinity	Petrography
LL-54	Lamprophyre (minette)	Hypabyssal	SiO_2-undersat.	cpx + kfs + phl ± ap + (ol) + (plg) + mag + ilm + ep + rt
LL-31	Lamprophyre (minette)	Hypabyssal	SiO_2-undersat.	kfs + cpx + ol ± mag + ilm + phl
LL-12	Lamprophyre (kersantite)	Hypabyssal	SiO_2-undersat.	cpx + plg + kfs + phl ± ap + (ol) + mag + ilm + ep + rt
LD-1	Phonolite	Hypabyssal	SiO_2-undersat.	kfs + ne + plg + phl ± mag + ilm + zrn + zrc + thr
LD-5	Trachyte	Hypabyssal	SiO_2-sat.	kfs + plg + cpx + phl + hbl ± qz + ap + mag + ilm
LL-52B	Trachyte	Hypabyssal	SiO_2-sat.	kfs + plg + phl ± rbk + sid + sdl + mag + ilm + zrn + zrc + thr
LL-58	Shonkinite	Intrusive	SiO_2-undersat.	kfs + cpx + phl + plg + ne + ap ± mag + ilm
LS-32	Nepheline-syenite	Intrusive	SiO_2-undersat.	kfs + plg + cpx + phl + ne + ap ± mag + ilm
LS-55	Nepheline-syenite	Intrusive	SiO_2-undersat.	kfs + cpx + phl + ne ± ap + mag + ilm
LS-24	Syenite	Intrusive	SiO_2-sat.	kfs + plg + cpx + phl + hbl ± qz + ap + mag + ilm
LM-12	Monzonite	Intrusive	SiO_2-oversat.	kfs + qz + plg + hbl + cpx ± ttn + ap + mag + ilm + zrn + ep

4.1.1.2. Felsic dykes. Felsic dykes show phaneritic to aphanitic textures ranging from porphyritic to granular hypidiomorphic, with K-feldspar over plagioclase in abundance.

Phonolites are aphanitic in texture, characterized by an association of anhedral K-feldspar, with perthitic exsolutions, and nepheline with minor plagioclase and mica (Fig. 3d). Groundmasses are made up by K-feldspar, nepheline and plagioclase with accessory Fe-Ti oxides, zircon, zirconolite, and thorite occurring as interstitial crystals and as inclusions in the main mineral phases. Nepheline shows a diffuse alteration to cancrinite and felspar a slight alteration in sericite.

Trachytes have porphyritic textures passing gradually to granular hypidiomorphic. The porphyritic end member (sample LD-5) shows K-feldspar, plagioclase, clinopyroxene, phlogopite, and hornblende phenocrysts surrounded by a micro-crystalline groundmass mainly made of K-feldspar, plagioclase with rare quartz (Fig. 3e). Fe-Ti oxides and apatite are the main accessory minerals. Chlorite and sericite are present as secondary minerals after mica/amphibole and feldspar, respectively. The granular end member (sample LL-52B) shows a granular texture and

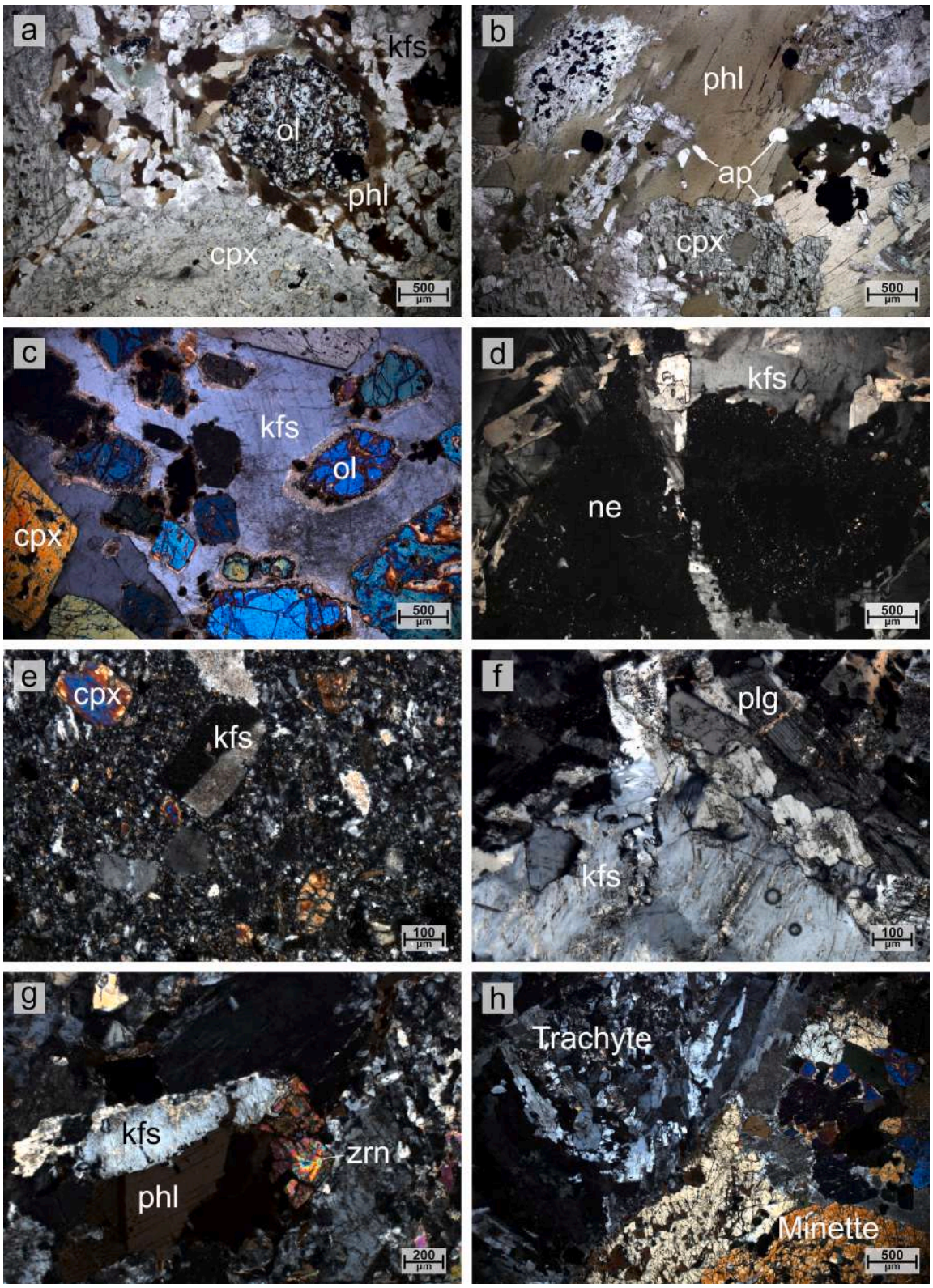

Fig. 3. Petrographic features of subvolcanic hypabyssal rocks from the Lar Complex (SE Iran). a) Lamprophyric rocks are characterized by large clinopyroxene phenocrysts and by phlogopite and K-feldspar in the groundmass, and ultramafic enclaves (up to 4 mm), made up of clinopyroxene and minor oxides microcrystals and rimmed by phlogopite, are present in some samples. b) Phlogopite in lamprophyres occurs both disseminated (as phenocrysts or in the groundmass) and included in clinopyroxene. c) Poikilitic K-feldspar crystals including olivine and clinopyroxene with reaction borders. d) Association of anhedral K-feldspar and nepheline with minor plagioclase in a phonolite. e) K-feldspar, clinopyroxene, and phlogopite phenocrysts surrounded by a crypto-crystalline groundmass in the trachytic porphyritic end member. f-g) K-feldspar with perthitic exsolution and minor plagioclase and phlogopite in the trachytic granular end-member; sub-millimetric zircon appears as accessory mineral. h) Close-up of the clear contact border between the trachytic granular end-member (left) and the lamprophyre (right). Minerals abbreviations after Whitney and Evans (2010).

is constituted by K-feldspar, plagioclase, and minor phlogopite (Fig. 3f). K-feldspar shows, similarly to phonolites, perthitic exsolutions. Accessory minerals are riebekite, siderophyllite, zircon (Fig. 3g), zirconolite, sodalite and magnetite, with ilmenite exsolutions and thorite inclusions. This sample intrudes an alkali minette without reactions at the contact (Fig. 3h).

4.1.2. Intrusive rocks

Intrusive rocks have clear phaneritic, medium- to coarse-grained hypidiomorphic textures independently of their mineralogy and degrees of silica saturation.

4.1.2.1. Nepheline-syenites and Shonkinite. Nepheline-syenites are divided, on a textural basis, into coarse-grained poikilitic and fine-grained porphyritic sub-groups.

The poikilitic nepheline-syenite is characterized by K-feldspar megacrysts (up to 2–3 cm), including abundant subhedral phlogopite and clinopyroxene, and minor Fe-Ti oxides and plagioclase. Clinopyroxene is present both as micro-phenocryst (up to 2 mm), like those found in lamprophyres, with abundant phlogopite inclusions and corroded borders, and with poikilitic texture (up to 0.5 mm) enclosed in K-feldspar (Fig. 4a). Nepheline occurs as intergrowths with smaller K-feldspar. Euhedral crystals of apatite (up to 0.7 mm) occur as inclusions in all mineral phases, suggesting early apatite precipitation. Ultramafic enclaves (up to 2 mm), entirely made of clinopyroxene microcrystals, always rimmed by phlogopite, are also present.

The porphyritic nepheline-syenite is characterized by complex feldspar macrocrysts (up to 4 cm) with plagioclase (up to 0.8 mm) core mantled by K-feldspar overgrowths showing an anti-rapakivi texture (Fig. 4b). The K-feldspars rims host many inclusions (clinopyroxene, phlogopite, and plagioclase), aligned closely the crystal edge, and present perthitic exsolutions. Clinopyroxene is present both as large phenocrysts (up to 4 mm) including abundant phlogopite microcrystals and as inclusion free smaller crystals (up to 0.5 mm), similar to those found in poikilitic nepheline-syenites. Phlogopite phenocrysts are characterized by elongated habitus with corroded borders, rarely altered in chlorite. Euhedral crystals of apatite (up to 0.7 mm) and Fe-Ti oxides occur as inclusions in all mineral phases. The groundmass is fine-grained and mainly characterized by anhedral K-feldspar, and minor plagioclase and nepheline. The presence of K-feldspar both as phenocryst and in the groundmass suggests two generations of K-feldspar.

A couple of samples (*i.e.*, samples LS-55 and LS-54) show different macroscopic features compared with the porphyritic Ne-syenite subgroup, since they are characterized by a distinctly darker colour and by the scarcity of K-feldspar macrocrysts. Moreover, the thin section observation of these samples reveals the absence of plagioclase phenocrysts and the presence of a peculiar texture characterized by nepheline and K-feldspar intergrowths (Fig. 4c).

Sample LL-58 slightly differs from other nepheline-syenites by the greater presence of large clinopyroxene phenocrysts, possibly of cumulus origin, with abundant inclusions of phlogopite, which can be classified as shonkinite (Fig. 4d).

4.1.2.2. Syenites. Syenites are porphyritic in texture with K-feldspar, plagioclase, clinopyroxene, phlogopite, and hornblende phenocrysts surrounded by a fine-grained groundmass mainly made of K-feldspar, plagioclase with rare quartz. Fe-Ti oxides and apatite are the main accessory minerals (Fig. 4e). K-feldspar and plagioclase are often found in glomeroporphyric aggregates, with an anti-rapakivi texture, and commonly show apatite, clinopyroxene and phlogopite inclusions. Chlorite and sericite represent the most common alteration phases on mica/amphibole and feldspar, respectively.

4.1.2.3. Monzonites. Monzonites are characterized by granular to porphyritic texture with large K-feldspar macrocrysts (up to 3 cm) included in a fine- to medium-grained groundmass. K-feldspar macrocrysts, pinkish in hand sample, host many inclusions toward the crystal rims that, in parallel, become outward progressively more altered to sericite. These macrocrysts show oscillatory zoning and perthitic exsolutions. Phenocrysts of smaller grain size consist of plagioclase (Fig. 4f), hornblende (Fig. 4g) and clinopyroxene, whereas the groundmass is made of phlogopite, hornblende, K-feldspar and quartz (Fig. 4h). Plagioclase shows oscillatory zoning. Accessory minerals are mainly represented by titanite (up to 2 vol%) and by minor magnetite, with ilmenite exsolutions, apatite, zircon, and epidote. Plagioclase and K-feldspar are often altered to sericite, clinopyroxene in amphibole, whereas chlorite alteration mainly characterizes mica.

4.2. Whole-rock major and trace elements geochemistry

Representative major and trace element compositions of intrusive to sub-volcanic rocks of the Lar Igneous Complex are reported in Table 3 (see Table S1 for the complete data set).

From a rigorous classification perspective, the hypabyssal to intrusive rocks of Lar Igneous Complex need to be characterized using both chemical and mineralogical features. Indeed, using the chemical scheme proposed by Le Maitre, 2002, Fig. 5a), the hypabyssal to intrusive Lar's rocks range in composition from gabbro to foiditic gabbro and monzodiorite for the lamprophyres, from syenite to foiditic syenite for felsic dykes, and from foiditic monzosyenite, to syenite, monzonite and quartz-monzosyenite for intrusive terms. On the other hand, this classification might be misleading when aphanitic rather than phaneritic rocks are considered. Felsic dykes, in our opinion are better described in terms of petrographic and chemical features as phonolite and trachyte rather than syenite *sensu lato*, which better applies for a granular silica-saturated rocks. In addition, most of mafic hypabyssal rocks have textures and mineralogies that indicate they are lamprophyres, as already indicated in recent literature (*e.g.*, Boomeri et al., 2020; Sargazi et al., 2022). These lamprophyres using mineralogical composition fall well within the field of calc-alkalic (shoshonitic) lamprophyres and are classified as minette and kersantite (Le Maitre, 2002).

The Lar Igneous Complex displays also a variable K_2O content (2.36–7.94 wt%) and a K_2O/Na_2O of 0.6–2.7. When plotted in the SiO_2 *vs* K_2O diagram (Peccerillo and Taylor, 1976) and in the Na_2O *vs* K_2O for the classification of potassic rocks (Fig. 5b-c), they show shoshonitic to ultrapotassic affinity. In particular, lamprophyres and nepheline-syenites show the highest K_2O/SiO_2 ratio (up to 0.14) straddling the boundary between potassic and ultrapotassic rocks, whereas monzonites (0.07–0.08), trachytes, and syenites (0.08–0.10) show a lower alkalinity. The occurrence of a nepheline-syenite with high abundance of clinopyroxene and phlogopite phenocrysts speaks for a shonkinite among intrusive rocks.

In the A/CNK *vs* A/NK binary plot all the investigated rocks show a peraluminous composition with exception of lamprophyres and shonkinite, which are metaluminous instead (Fig. 5d).

The distribution of major oxides with respect to the MgO content (on anhydrous basis) of the Lar igneous complex is shown in Fig. 6. A progressive decrease of TiO_2, Fe_2O_3 and CaO with decreasing MgO is generally observed (Fig. 6a-b-c). On the other hand, Al_2O_3 shows a general increase with decreasing MgO, and a well-defined trend is depicted by lamprophyres, nepheline-syenites, and phonolite samples (characterized by the highest Al_2O_3 values, up to 23.5 wt%). Monzonites, syenites, and trachytes do not belong to this trend showing lower alumina at comparable MgO content (Fig. 6d). The K_2O distribution shows an enrichment from lamprophyres to nepheline syenites, the latter having the highest K_2O content of the whole dataset (up to 7.94 wt % at MgO around 2 wt%). Monzonites and syenites/trachytes reach lower maximum K_2O contents of 5.25 and 6.35 wt% at comparable MgO, whereas phonolites and the more evolved trachytic dykes show a decrease of K_2O values compatible with the fractionation of K-rich phase at the final stages of differentiation (Fig. 6e). Na_2O displays a general

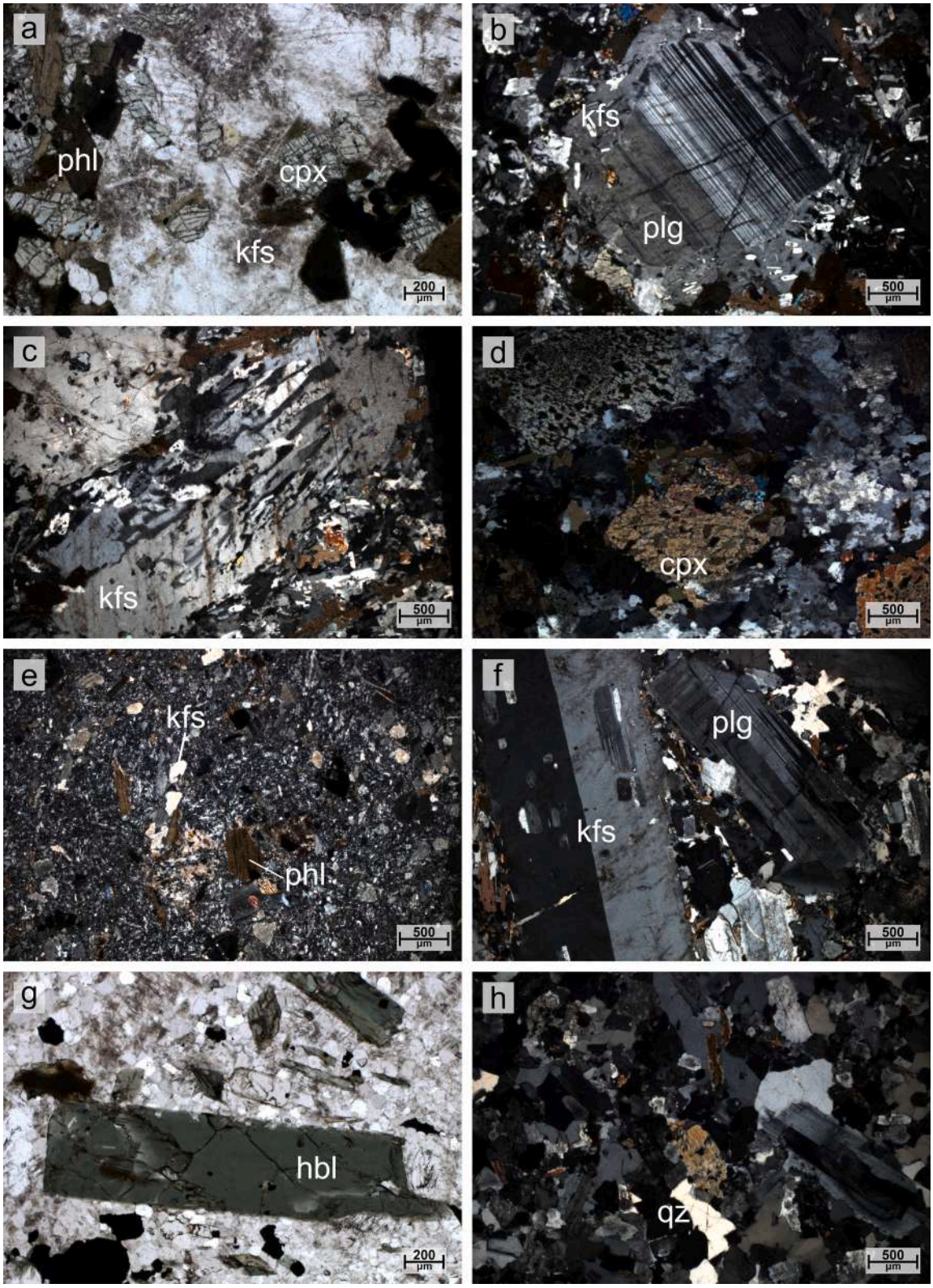

Fig. 4. Petrographic features of intrusive rocks from the Lar Complex (SE Iran). a) Poikilitic nepheline-syenite with K-feldspar megacrysts including phlogopite and clinopyroxene crystals. b) Anti-rapakivi texture with plagioclase at the core, rimmed by K-feldspar overgrowths displaying clinopyroxene, phlogopite, and plagioclase inclusions. c) K-feldspar and nepheline intergrowths in a ne-syenite. d) Shonkinite sample characterized by a greater presence of large clinopyroxene phenocrysts, with phlogopite inclusions. e) Syenites sample with K-feldspar, plagioclase, clinopyroxene, phlogopite, and hornblende phenocrysts surrounded by a fine-grained groundmass mainly made of K-feldspar, plagioclase with rare quartz. Large megacrysts of K-feldspar (f), plagioclase (f) and hornblende (g) in a groundmass mad of phlogopite, hornblende, K-feldspar and quartz (h) in monzonite. Minerals abbreviations after Whitney and Evans (2010).

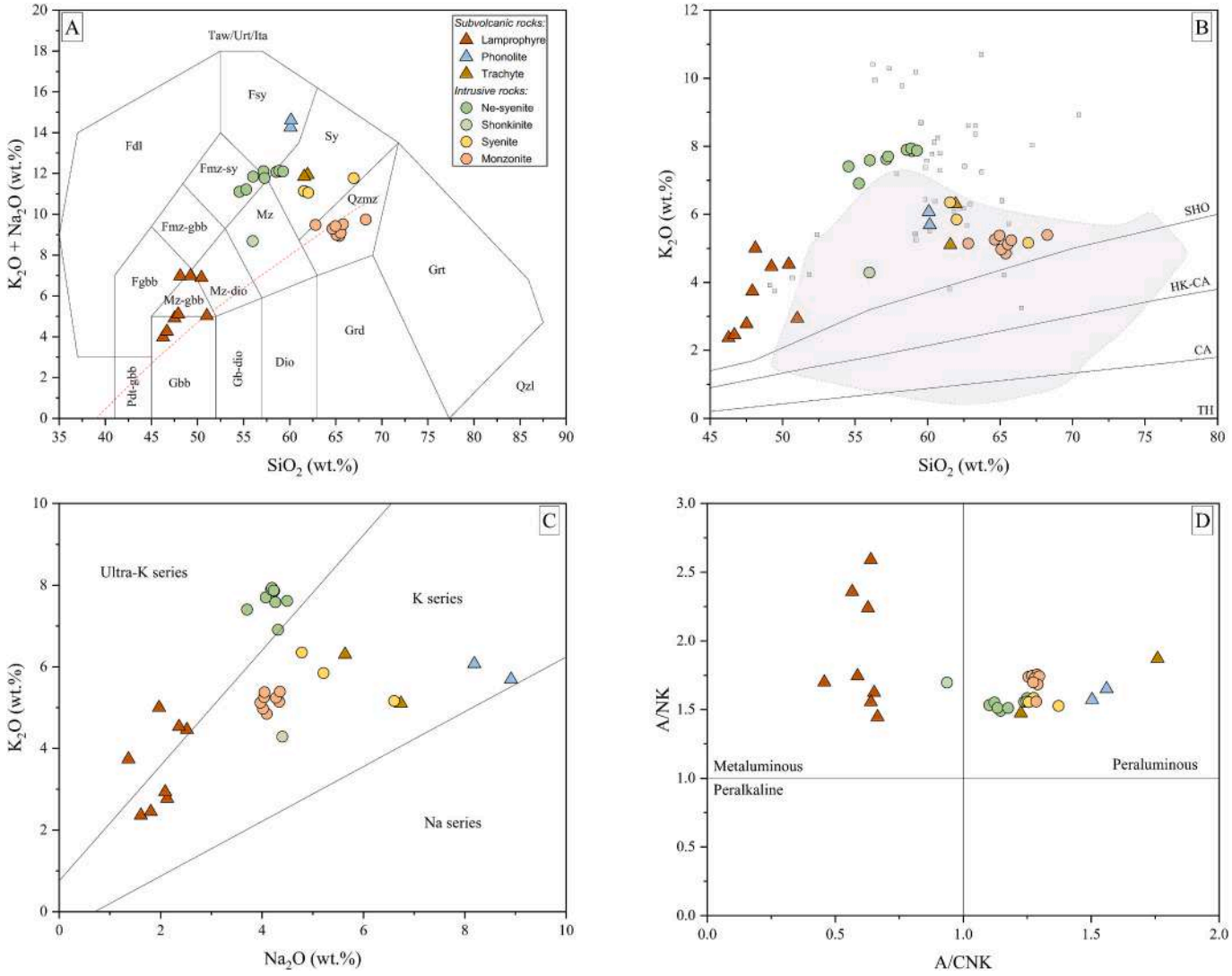

Fig. 5. (A) TAS (Le Maitre et al., 2002), (B) K_2O *vs* SiO_2 (Peccerillo and Taylor, 1976), (C) Na_2O *vs* K_2O and (D) A/CNK *vs* A/NK classification diagrams of igneous rocks from the Lar Complex (SE Iran). Pdt-gbb – peridot-gabbro; Gbb – gabbro; Gb-dio – gabbro-diorite; Dio –diorite; Grd – granodiorite; Grt – granite; Qzl – quartzolite; Mz-gbb – monzo-gabbro; Mz-dio – monzo-diorite; Mz – monzonite; Qzmz – quartz-monzonite; Sy – syenite; Fgbb – foid-gabbro; Fmz-gbb – foid-monzo-gabbro; Fmz-sy – foid-monzo-syenite; Fsy – foid-syenite; Fdl – foidolite; Taw/Urt/Ita – tawite/urtite/italite; TH – tholeiitic series; CA – calc-alkaline series; HK-CA – high-K calc-alkaline series; SHO – shoshonite series. Dashed grey field in the (B) K_2O *vs* SiO_2 diagram includes data from different igneous complexes along the Sistan Suture Zone (Arjmandzadeh et al., 2011; Pang et al., 2013; Kosh Kolg et al., 2017; Mohammadi et al., 2016; Omidianfar et al., 2020; Sargazi et al., 2022), while grey squares represent data from past studies on the Lar Complex (Boomeri et al., 2019, 2020; Sargazi et al., 2022).

increase at decreasing MgO, reaching a peak in phonolites (8.9 wt%). Monzonites show comparatively low sodium content displacing from the general trend defined by the other lithotypes (Fig. 6f). P_2O_5 shows scattered but broadly increasing values at decreasing MgO in lamprophyres, it reaches the maximum content of 1.32 wt% in the least evolved nepheline-syenites (MgO around 4 wt%) and it is characterized by a sharp decrease at progressively lower MgO content probably due to the significant apatite fractional crystallization (Fig. 6g).

The two distinct liquid lines of descent (LLD) trends defined by the major element distribution of the monzonites-syenites-trachytes and of the lamprophyres-nepheline-syenites-felsic dykes suites are also highlighted by trace elements. Cr, Ni, Co and Sc show a positive correlation with MgO, with lamprophyres characterized by the highest contents, especially in samples containing the greatest amount of olivine (Ni up to 490 $\mu g \bullet g^{-1}$, Cr up to 1240 $\mu g \bullet g^{-1}$, Fig. 7a-b) and of clinopyroxene (Sc up to 47 $\mu g \bullet g^{-1}$, Fig. 7c). On the other hand, felsic dykes show the lowest values of these compatible elements as they represent the most evolved samples. The distribution of V ($\mu g \bullet g^{-1}$) mimics that of TiO_2 (wt %) plausibly reflecting the fractional crystallization of Fe-Ti oxides (Fig. 7d).

The most incompatible elements such as Th and Zr (Fig. 7e-f) display a gradual increase (Th from 1.43 to 25.6 $\mu g \bullet g^{-1}$, Zr from 34 to 216 $\mu g \bullet g^{-1}$) at decreasing MgO down to values of *ca.* 2 wt%, followed by a sharp increase in trachytes and phonolites (Th up to 285 $\mu g \bullet g^{-1}$, Zr up to 1734 $\mu g \bullet g^{-1}$). This hyperbolic enrichment trend appears to be defined by all the Lar's rocks (apart from monzonites), show Th and Zr concentrations of 6.79–11.3 and 78–102 $\mu g \bullet g^{-1}$, respectively.

The primitive mantle (Sun and McDonough, 1989) incompatible elements and the chondrite (Sun and McDonough, 1989) normalized Rare Earths Elements (REE) distributions of Lar's rocks are presented in Fig. 8. All the samples investigated are characterized by marked Nb, Ta, and Ti troughs and Pb peaks, suggesting a derivation from a subduction-related magmatic event (*e.g.*, Hofmann, 1997). In particular, lamprophyres (Fig. 8a) show high LILE/HFSE values, enrichments in Ba, K and Pb, troughs in Th, U, Nb, Ta, Zr, Hf, and Ti, and Ba/Th ranging from 140 to 1034. Their REE distribution is characterized by moderate LREE/

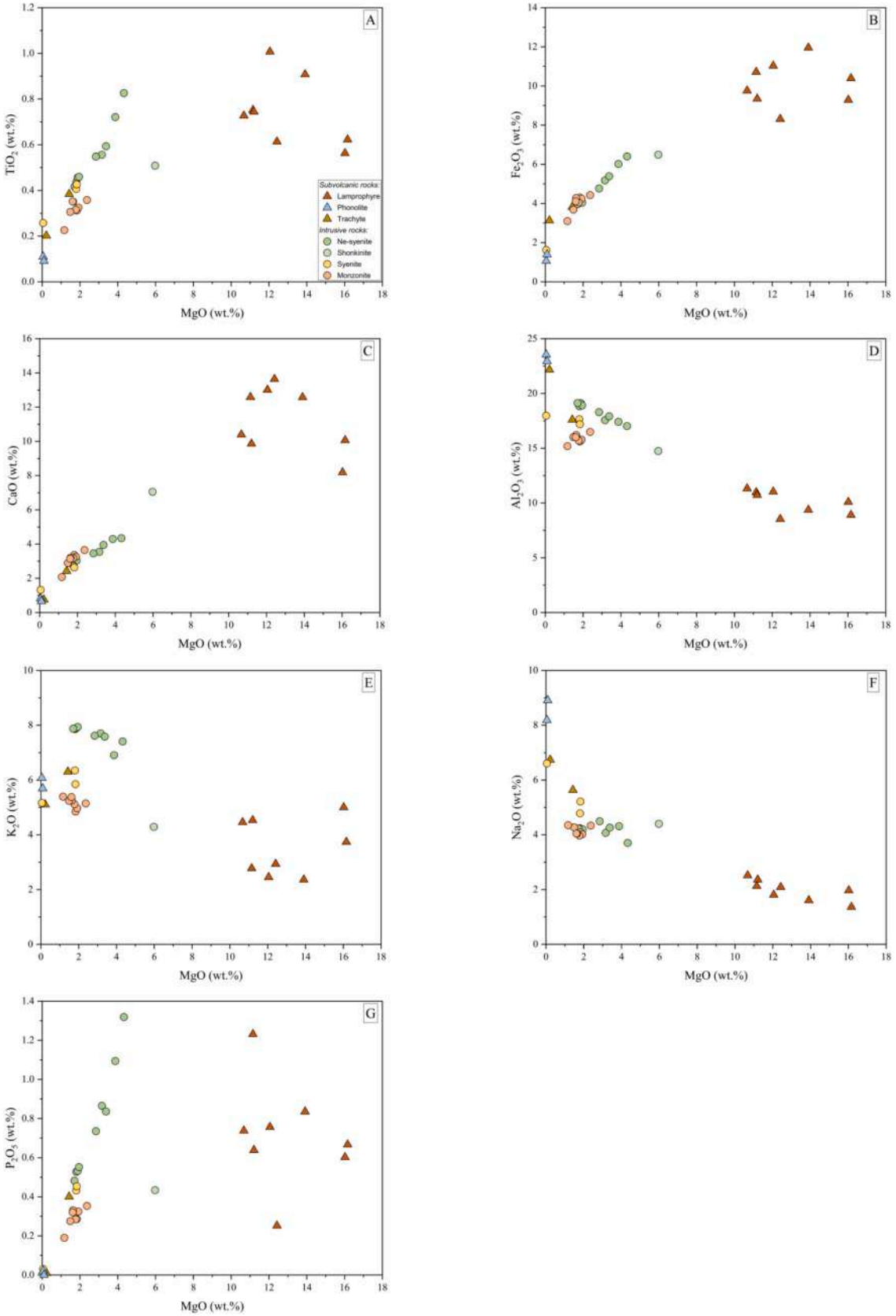

Fig. 6. Major element *versus* MgO (wt%) bivariate diagrams of igneous rocks from the Lar Complex (SE Iran).

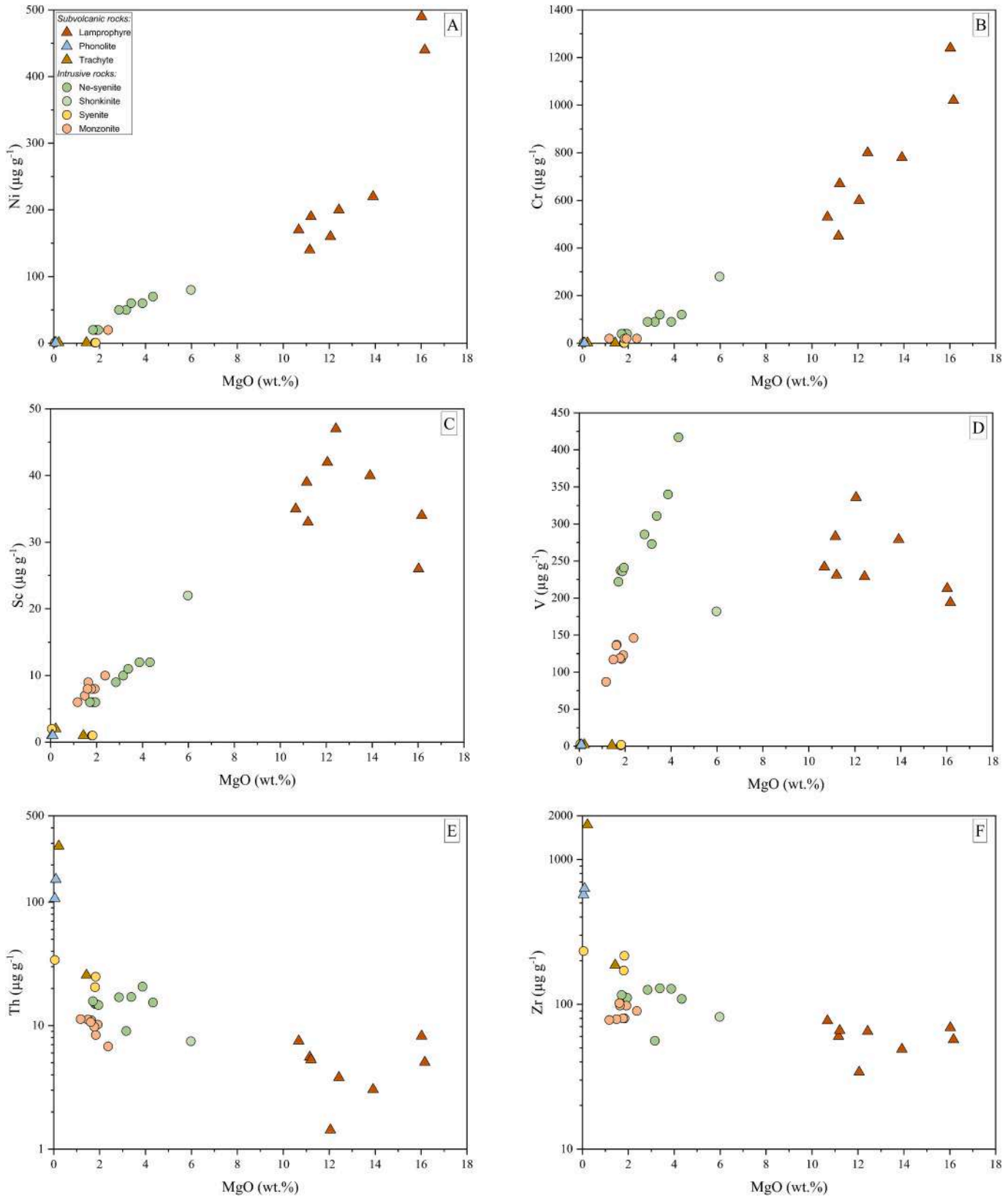

Fig. 7. Trace element *versus* MgO (wt%) bivariate diagrams of igneous rocks from the Lar Complex (SE Iran).

HREE fractionation (La_N/Yb_N = 10.0–15.7), a weak Eu negative anomaly (median value 0.87) and by La_N/Sm_N ranging from 1.7 to 3.2 (Fig. 8f).

Phonolitic dykes show incompatible elements and REEs distributions very different from the other lithotypes, possibly due to their extreme differentiation degree. In fact, they show very high concentrations of incompatible elements such as Pb, Th, U, Hf, and Zr, which do not enter the fractionated minerals. On the contrary, elements entering the crystal

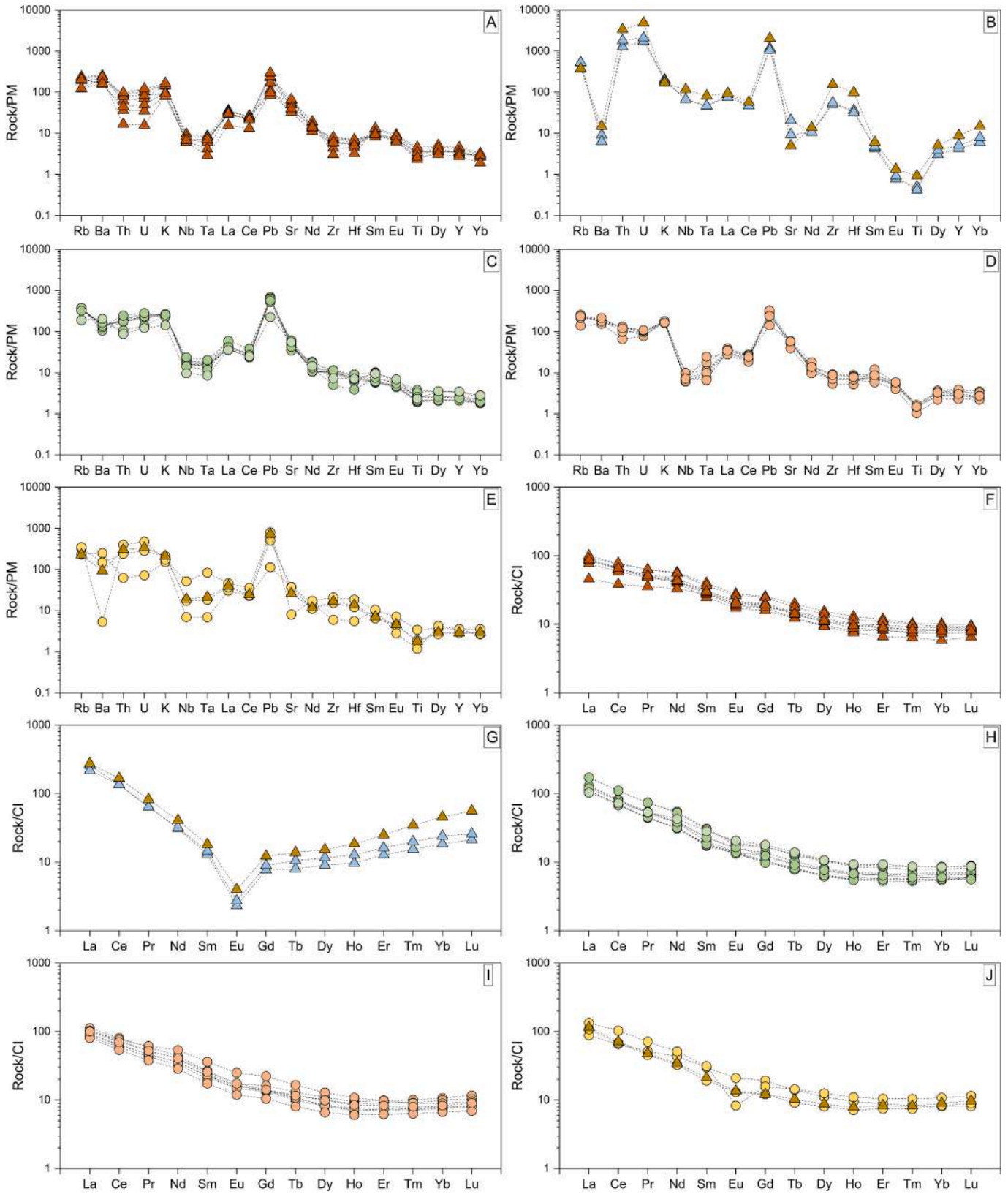

Fig. 8. Primitive mantle-normalized (Sun and Sun and McDonough, 1989) incompatible element patterns of a) lamprophyre, b) phonolite (with LL-52B trachyte), c) ne-syenites, d) monzonite, e) syenite (with LD-5 trachyte) and chondrite-normalized (Sun and Sun and McDonough, 1989) Rare Earths Elements distributions of f) lamprophyre, g) phonolite (with LL-52B trachyte), h) ne-syenites, i) monzonite, j) syenite (with LD-5 trachyte) rock from Lar Complex (SE Iran).

lattice of feldspar, titanite and Fe-Ti oxides such as Ba, Eu, Sr, and Ti show very low concentrations (Fig. 8b). The REE distribution of phonolitic dykes (Fig. 8g) show a U-shaped pattern characterized by high LREE (La_N = 200–300 times chondrite) and HREE (Yb_N = 20–40 times chondrite) and by a strong Eu negative anomaly (Eu/Eu* = 0.23, average value, with $Eu^* = \sqrt{(Sm \times Gd)_N}$), which are probably due to the fractionation of titanite and plagioclase, respectively. A trachytic dyke (LL-52B) shows very similar incompatible elements and REEs patterns to the phonolitic dykes.

Nepheline-syenites show an incompatible elements pattern (Fig. 8c) very similar to lamprophyres, with a comparatively higher concentration of the most incompatible elements during early magmatic differentiation, resulting in attenuated troughs in Nb, Ta, Zr, Hf and Ti and more pronounced peaks in Rb and Pb. Their REEs pattern (Fig. 8h) is characterized by a comparatively high REE fractionation (La_N/Yb_N = 19.2–22.9), La_N/Sm_N from 5.5 to 6.7 and by a more pronounced Eu negative anomaly especially in the least differentiated samples (MgO > 2.82 wt%).

Monzonites (Fig. 8d) have a distribution of incompatible elements similar to nepheline-syenites, but displaying a more pronounced Nb, Ta and Ti negative anomalies. Their REE patterns (Fig. 8i) show a distinctly lower LREE over HREE fractionation with respect to those of nepheline-syenites (La_N/Yb_N = 10.9–12.7) coupled with a lower La_N/Sm_N (3.8–4.8).

The incompatible elements distribution of syenites (Fig. 8e) and of the trachytic dyke LD-5 is similar to that of other lithotypes apart from a marked positive anomaly in Ba, which progressively increases from LM-51 to LS-56 with the degree of differentiation. Their REEs patterns (Fig. 8j) are also very similar (La_N/Sm_N = 4.28; Tb_N/Yb_N = 1.39; La_N/Yb_N = 12.07), except for a marked Eu anomaly in sample LS-56 (Eu/Eu* = 0.37) suggesting significant plagioclase fractionation, which is not generally present in all other syenite samples. LM-51 and LS-56 are more enriched in MREEs.

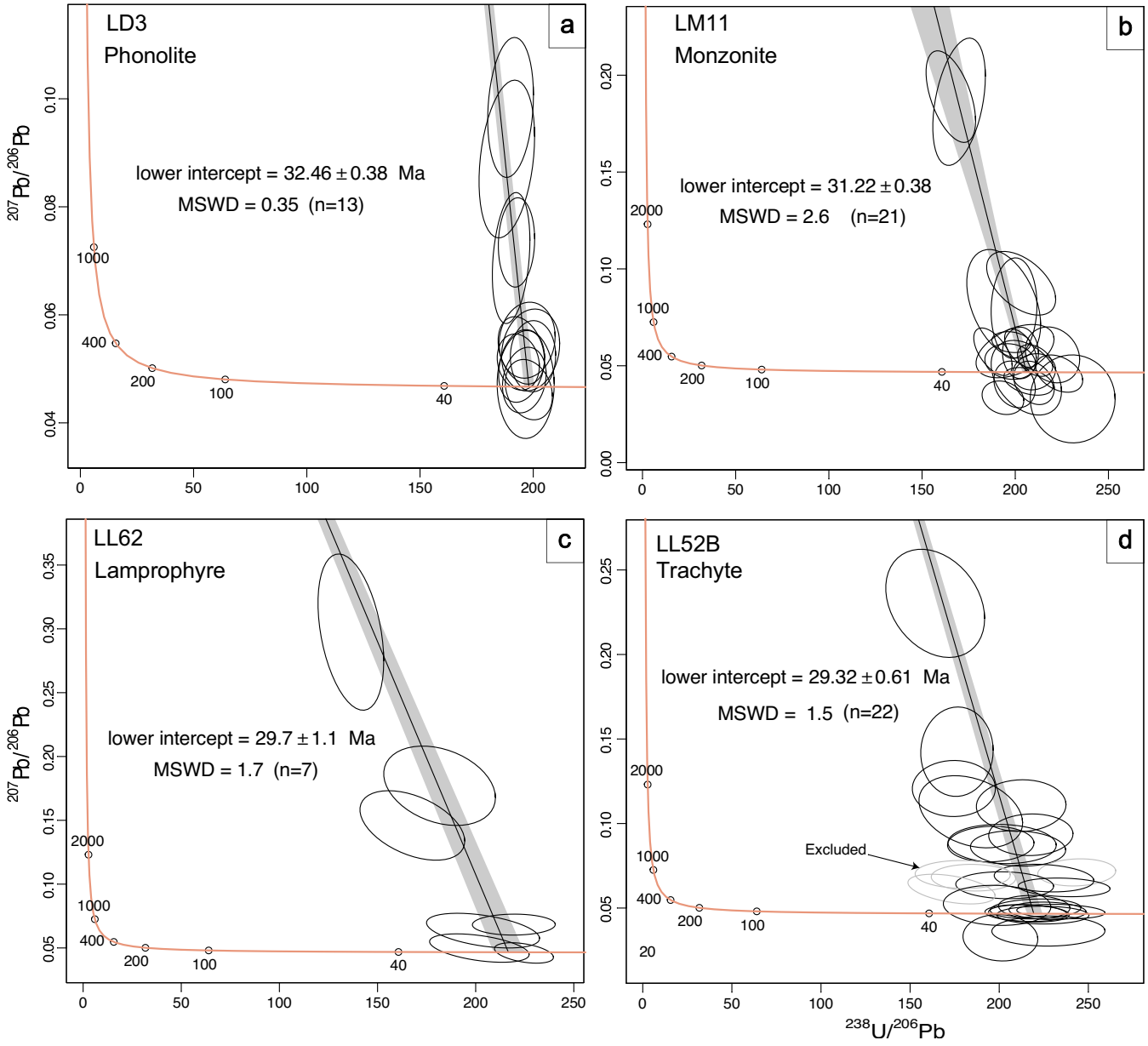

Fig. 9. U-Pb Discordia diagrams as obtained from the *in-situ* zircon dating of the studied magmatic rock samples.

4.3. U-Pb Geochronology

4.3.1. Zircon samples (LD-3 phonolite, LM-11 monzonite, LL62 and LL52B lamprophyres)

Zircon grains from the phonolite sample LD3 are subhedral to euhedral, ranging from 50 to 200 μm in size. Some crystals exhibit well-developed pyramidal terminations and typically display length-to-width ratios of approximately 1.5:1 to 4:1 (Fig. S1a). Most grains exhibit strongly resorbed, often fractured, margins. An original oscillatory zoning is present but frequently truncated by alteration halos, leading to a heterogeneous texture. Alteration halos are typified by abundant (~5–15 vol%) thorite and feldspar inclusions. The zircon grains are highly Th-rich, containing ~15,700–44,000 ppm Th and displaying extremely Th/U values between 27.9 and 71.5 (Kirkland et al., 2015), consistent with thorian zircon compositions. Owing to alteration, most of the analyzed spots provided discordant ages. A Discordia age of 32.46 ± 0.38 Ma (2σ; MSWD = 0.35, n = 13) is obtained on Tera-Wasserburg plot (Fig. 9a; Table 2).

Zircon grains of the monzonite sample LM-11 are predominantly euhedral, ranging in size from 15 to 60 μm. Their morphology is characterized by pyramidal habits with minor occurrences of prismatic forms with length-to-width ratios typically between 1:1 and 2:1. Texturally, most grains are homogeneous, displaying oscillatory zoning. While some grains exhibit fracturing, they are rarely associated with inclusions and generally maintain intact margins with preserved internal oscillatory zoning (Figs. S1b). The zircons have high Th contents (~500–10,000 ppm), corresponding to Th/U values between 2.89 and 7.24. A Discordia age of 31.22 ± 0.38 Ma (2σ; MSWD = 2.6, n = 21) was obtained in the Tera-Wasserburg plot (Fig. 9b; Table 2).

Zircon grains of the lamprophyre sample LL-62 are predominantly anhedral to subhedral, ranging in size from 15 to 70 μm. Their morphology is mainly characterized by elongated habits, with minor occurrences of prismatic forms. Length-to-width ratios are highly variable, typically falling between 1:1 and 6:1. Most grains are intensely fractured, displaying resorbed and rounded margins. The original oscillatory zoning is rarely preserved, overprinted by diffuse alteration. Thorite inclusions are rarely observed. The zircons exhibit high Th contents (ranging ~400–34,000 ppm), corresponding to Th/U values ranging between 1.75 and 12.93. Given the pervasive alteration, most analyzed spots yielded discordant ages. A Discordia age of 29.7 ± 1.1 Ma (2σ; MSWD = 1.7, n = 7) was obtained on Tera-Wasserburg plot (Fig. 9c; Table 2).

Zircon grains of the lamprophyre sample LL-52B are subhedral to euhedral and range in size from 15 to 220 μm. Their morphology is predominantly short prismatic, though some exhibit pyramidal habits. The length-to-width ratios typically range from 1:1 to 3:1. The zircon population can be divided into two main groups of grains based on textural features and alteration: (i) grains that are predominantly subhedral, characterized by resorbed rims like those observed in sample LD3. These zircons are strongly altered, displaying residual traces of oscillatory zoning. They commonly contain abundant thorite inclusions and vugs (Fig. S1c); and (ii) grains showing partial alteration, mainly restricted to the core, characterized by a distinct rimward overgrowth zone. A few grains within this group exhibit more homogeneous, well-developed oscillatory zoning (Fig. S1d). Most of the analytical spots were focused on the inclusion-free zones the zircons. The Th contents of these zircons range between ~17 and 6282 ppm, corresponding to Th/U values of 0.06 to 7.71. Also in this case, most of the analyzed spots provided discordant ages, resulting in a Discordia age of 29.32 ± 0.61 Ma (2σ; MSWD = 1.5, n = 22) on Tera-Wasserburg plot (Fig. 9d; Table 2).

4.3.2. Apatite samples (LS-29 nepheline sienite, LL-52A and LL-62 lamprophyres)

Apatite grains are generally euhedral to subhedral and range in size from 50 to 400 μm. Their morphology is characterized by hexagonal, elongated, and prismatic habits. The length-to-width ratios are highly variable, often exceeding 10:1 for elongated crystals. The modal abundance of apatite varies between the samples, with samples LS29 and LL52A showing 1–2 vol%, while sample LL62 exhibits a higher abundance of 3–4%. Apatite occurrence also varies significantly by sample. In sample LL52A, apatite primarily occurs as inclusions within phenocrysts. In sample LS29, apatite is mainly dispersed throughout the groundmass. In sample LL62, apatite is predominantly distributed along the margins of phenocrysts and is frequently associated with phlogopite grains. In all samples, BSE imaging reveals homogeneous apatite compositions (Fig. S1). Using the Tera-Wasserburg plot, Discordia ages of 32.0 ± 2.0, 30.41 ± 0.92, and 30.3 ± 1.1 Ma (2σ) were calculated for samples LS29, LL-52A and LL-62, respectively (Fig. 10; Table 2).

4.3.3. K-Ar whole rock dating

Whole-rock K-Ar dating of the nepheline syenite sample LS-55 yielded an age of 32.2 ± 0.7 Ma. A slightly younger K-Ar age of 31.1 ± 0.8 Ma was obtained for the monzonite sample LM-14, whereas the youngest age within the suite, 22.8 ± 0.7 Ma, was determined for the syenite sample LS-56 (Table 2).

4.4. Sr-Nd-Pb isotopes

The results of Sr-Nd-Pb isotopic analyses of selected Lar's rocks are reported in Table 4. Initial $^{87}Sr/^{86}Sr$ and $^{143}Nd/^{144}Nd$ values vary from 0.704296 to 0.706213 and from 0.512627 to 0.512748 (εNd from −0.09 to 2.27), respectively. In the $^{87}Sr/^{86}Sr_i$ *vs* $^{143}Nd/^{144}Nd_i$ bivariate diagram the samples plot invariably near the composition of the Bulk Silicate Earth (Fig. 11), except for three samples, a syenite, a trachyte, and a phonolite, displaying more radiogenic Sr and less radiogenic Nd. The composition of Lar's rocks is similar to that of other Oligocene plutons (inset of Fig. 11) – *e.g.,* Chah-Shaljami granitoids (Arjmandzadeh et al., 2011b), Dehsalm granitoids (Arjmandzadeh and Santos, 2014), Koudakan intrusion (Omidianfar et al., 2020), multiple Lut-Sistan igneous

Table 2
Results of *in-situ* LA-ICP-MS U-Pb dating on zircons and apatites in thin section, along with K/Ar analysis of whole-rock samples. Lamp = Lamprophyre; Sho = Shonkinite; Ne-sy = Nepheline-syenite; Pho = Phonolite; Mz = Monzonite; Sy = Syenite; Trach = Trachyte.

Sample	LL-52A	LL-62	LL-62	LS-29	LS-55	LD-3	LM-11	LM-14	LS-56	LL-52B
Lithology	Hypabyssal	Hypabyssal	Hypabyssal	Intrusive	Intrusive	Hypabyssal	Intrusive	Intrusive	Intrusive	Hypabyssal
Affinity	SiO_2-undersat.	SiO_2-undersat.	SiO_2-undersat.	SiO_2-undersat.	SiO_2-undersat.	SiO_2-undersat.	SiO2-oversat.	SiO2-oversat.	SiO_2-oversat.	SiO_2-sat.
Rock type	Lamp	Lamp	Lamp	Ne-sy	Ne-sy	Pho	Mz	Mz	Sy	Trach
Method	U-Pb on apatite	U-Pb on apatite	U-Pb on zircon	U-Pb on apatite	K-Ar	U-Pb on zircon	U-Pb on zircon	K-Ar	K-Ar	U-Pb on zircon
Age	30.41	30.3	29.7	32.0	32.2	32.64	31.22	31.1	22.8	29.32
1 s.e.	0.92	1.1	1.1	2.0	0.7	0.38	0.38	0.8	0.7	0.61
MSWD	2.8	1.2	1.7	3.5		0.35	2.6			1.5
n	25	40	7	59		13	21			22

Table 3
Bulk rock major and trace elements composition of representative Oligocene igneous rocks from the Lar Complex Rock type, lithology, and affinity (SiO_2-undersaturated, SiO_2-oversaturated, and SiO_2-saturated) are also reported. Lamp = lamprophyre; Sho = Shonkinite; Ne-sy = Nepheline-syenite; Pho = Phonolite; Mz = Monzonite; Sy = Syenite; Trach = Trachyte.

Sample	LL- 12	LL- 31	LL- 54	LL- 58	LS- 32	LS- 55	LS- 59	LD- 1	LM- 12	LS- 24	LD- 5	LL- 52B
Lithology	Hypabyssal	Hypabyssal	Hypabyssal	Intrusive	Intrusive	Intrusive	Intrusive	Hypabyssal	Intrusive	Intrusive	Hypabyssal	Hypabyssal
Affinity	SiO_2-undersat.	SiO_2-undersat.	SiO_2-undersat.	SiO_2-undersat.	SiO_2-undersat.	SiO_2-undersat.	SiO_2-undersat.	SiO_2-undersat.	SiO_2-oversat.	SiO_2-sat.	SiO_2-sat.	SiO_2-sat.
Rock type	Lamp	Lamp	Lamp	Shonk	Ne-sy	Ne-sy	Ne-sy	Pho	Mz	Sy	Trach	Trach
SiO_2 (wt%)	47.08	47.13	44.84	55.47	58.10	55.60	58.28	59.15	62.26	61.25	60.33	61.40
TiO_2	0.75	0.55	0.88	0.50	0.43	0.59	0.45	0.11	0.36	0.40	0.37	0.20
Al_2O_3	10.88	9.88	9.08	14.61	18.57	17.78	19.03	23.17	16.34	17.56	17.14	22.10
Fe_2O_3	10.62	9.10	11.59	6.43	4.13	5.35	4.07	1.05	4.39	4.25	3.72	3.12
MnO	0.17	0.15	0.19	0.12	0.06	0.08	0.07	0.04	0.07	0.06	0.07	0.11
MgO	11.05	15.69	13.48	5.92	1.78	3.35	1.87	0.05	2.35	1.79	1.39	0.22
CaO	12.47	8.02	12.19	6.99	3.07	3.92	3.21	0.81	3.62	2.69	2.36	0.75
Na_2O	2.11	1.93	1.56	4.36	4.18	4.23	4.16	8.06	4.30	4.76	5.49	6.72
K_2O	2.75	4.90	2.29	4.25	7.75	7.53	7.86	5.98	5.10	6.32	6.14	5.09
P_2O_5	1.22	0.59	0.81	0.43	0.52	0.83	0.53	0.02	0.35	0.43	0.39	0.01
LOI	1.14	2.29	1.29	1.22	1.13	0.97	1.11	1.70	1.16	1.04	1.18	0.78
Sum	100.23	100.23	98.20	100.30	99.73	100.23	100.64	100.14	100.29	100.56	98.58	100.50
Sc (ppm)	39	26	40	22	6	11	6	< 1	10	8	7	2
Be	2	4	1	7	6	7	6	28	3	8	9	25
V	283	213	279	182	237	311	236	74	146	185	172	332
Cr	450	1240	780	280	40	120	40	< 20	20	30	20	< 20
Co	44	49	50	23	8	13	8	< 1	10	9	8	1
Ni	140	490	220	80	20	60	20	< 20	20	< 20	< 20	< 20
Cu	150	100	20	20	80	180	90	< 10	1980	860	120	20
Zn	70	60	80	40	40	50	40	< 30	< 30	30	40	70
Ga	13	10	12	14	15	14	15	30	15	15	15	30
Ge	1.4	1.3	1.7	1.4	1	1.1	0.9	1.4	1.4	1.2	1.1	1.7
As	6	< 5	< 5	< 5	6	6	6	16	< 5	5	< 5	15
Rb	88	130	77	121	221	237	227	329	134	208	143	236
Sr	1248	834	1324	1177	1029	960	1163	442	1402	777	547	106
Y	17.6	12.5	19.4	15.9	9.5	11.9	9.5	19.6	14.1	12.9	13	40.6
Zr	60	69	49	82	113	129	111	572	90	171	186	1734
Nb	5	4.9	5	6.9	11.4	12.8	11.3	47.5	4.8	12.2	13.6	83.9
Mo	4	3	< 2	< 2	2	12	3	3	< 2	3	< 2	2
Ag	< 0.5	< 0.5	< 0.5	< 0.5	< 0.5	< 0.5	< 0.5	2	< 0.5	0.8	0.6	4.7
In	0.1	< 0.1	0.1	< 0.1	< 0.1	< 0.1	< 0.1	< 0.1	< 0.1	< 0.1	< 0.1	< 0.1
Sn	1	1	1	1	1	1	1	1	1	1	1	1
Sb	0.30	0.20	< 0.2	0.20	0.40	0.60	0.30	1.50	0.20	0.30	0.30	1.50
Cs	5.80	4.50	2.00	7.90	8.90	12.6	9.30	35.0	2.70	5.00	2.30	14.0
Ba	1079	1159	1173	1418	939	975	1069	63	1662	1035	652	104
La	24.2	20.6	23.7	24.6	26.6	30.9	26.3	61.1	21.3	25.6	27.1	65.1
Ce	46.4	38.7	47.6	44.3	41.8	50.3	42.1	83.2	40.7	41.8	43.6	103
Pr	5.68	4.55	5.82	4.97	4.1	5.04	4.19	5.93	4.61	4.2	4.41	7.64
Nd	24.4	19	25.2	19.6	14.3	17.8	14.5	14.2	18.2	14.9	15.7	18.7
Sm	5.34	4.11	5.44	4.18	2.55	3.39	2.71	1.91	3.64	2.84	3.13	2.69
Eu	1.41	1.04	1.47	1.16	0.75	0.89	0.78	0.13	0.97	0.73	0.76	0.23
Gd	4.44	3.46	4.88	3.55	2.06	2.72	1.95	1.53	3.14	2.41	2.4	2.44
Tb	0.60	0.44	0.64	0.50	0.30	0.37	0.29	0.29	0.44	0.33	0.37	0.50
Dy	3.16	2.27	3.48	2.62	1.54	1.97	1.59	2.23	2.36	1.97	2.15	3.75
Ho	0.59	0.41	0.63	0.51	0.31	0.38	0.3	0.53	0.44	0.39	0.43	1.01
Er	1.56	1.06	1.75	1.49	0.91	1.09	0.9	2.04	1.31	1.19	1.33	3.99
Tm	0.22	0.16	0.24	0.21	0.14	0.17	0.14	0.38	0.19	0.18	0.20	0.85
Yb	1.44	0.94	1.51	1.37	0.90	1.12	0.92	2.96	1.35	1.34	1.44	7.36
Lu	0.23	0.16	0.23	0.21	0.14	0.17	0.15	0.53	0.21	0.22	0.24	1.38
Hf	1.60	1.60	1.40	2.20	2.10	2.50	2.30	11.30	2.20	3.70	4.20	30.5
Ta	0.27	0.29	0.25	0.35	0.62	0.64	0.61	1.85	0.29	0.75	0.87	3.35
W	8.60	2.00	0.60	0.80	1.00	2.90	2.80	2.80	1.00	3.90	2.40	3.10
Tl	< 0.05	< 0.05	< 0.05	0.06	0.18	0.17	0.19	0.28	0.1	0.22	0.12	0.11
Pb	10	21	6	16	45	46	45	83	17	36	51	145
Bi	< 0.1	0.1	< 0.1	0.1	0.2	0.2	0.2	0.6	0.5	0.6	0.3	0.6
Th	5.57	8.23	3.04	7.47	15.0	17.1	14.9	107	6.79	20.5	25.6	285
U	1.63	2.57	0.74	2.57	4.32	5.63	4.93	36.1	1.75	5.89	7.09	102

Table 4
Sr, Nd and Pb isotope composition of selected Oligocene igneous rocks from the Lar Complex and AGV-1. Both measured (m) and initial (i) values are reported. Rock type, lithology and affinity (SiO_2-undersaturated, SiO_2-oversaturated, and SiO_2-saturated) are also reported. Initial values were calculated using the average of the measured ages for each rock type. Age propagated errors (2 s.e.) are obtained by Montecarlo simulation. Lamp = Lamprophyre; Sho = Shonkinite; Ne-sy = Nepheline-syenite; Pho = Phonolite; Mz = Monzonite; Sy = Syenite; Trach = Trachyte.

Sample	LL-12	LL-31	LL-52A	LL-58	LS-55	LD-3	LM-12	LM-14	LS-24	LS-56	LL-52B	AGV-1
Lithology	Hypabyssal	Hypabyssal	Hypabyssal	Intrusive	Intrusive	Hypabyssal	Intrusive	Intrusive	Intrusive	Intrusive	Hypabyssal	
Affinity	SiO_2-undersat.	SiO_2-undersat.	SiO_2-undersat.	SiO_2-undersat.	SiO_2-undersat.	SiO_2-undersat.	SiO_2-oversat.	SiO_2-oversat.	SiO_2-sat.	SiO_2-sat.	SiO_2-sat.	
Rock type	Lamp	Lamp	Lamp	Shonk	Ne-sy	Pho	Mz	Mz	Sy	Sy	Trach	
Age (Ma)	30.30	30.30	30.10	32.20	32.20	32.77	32.35	32.35	22.80	22.80	27.19	
err	1.10	1.10	1.70	0.70	0.70	0.35	0.69	0.69	0.70	0.70	0.72	
Rb ($\mu g \bullet g^{-1}$)	88	130	133	121	237	334	134	139	208	221	236	
Sr	1248	834	685	1177	960	197	1402	827	777	169	106	
$^{87}Sr/^{86}Sr_m$	0.704384	0.704647	0.704539	0.704454	0.704848	0.708496	0.704568	0.704653	0.704888	0.706793	0.707552	0.703989
2se	0.000006	0.000006	0.000005	0.000006	0.000007	0.000005	0.000006	0.000006	0.000006	0.000005	0.000005	0.000006
$^{87}Rb/^{86}Sr$	0.2044	0.4521	0.5635	0.2979	0.7139	4.9249	0.2775	0.4865	0.7730	3.7829	6.4743	
$^{87}Sr/^{86}Sr_i$	0.704296	0.704452	0.704298	0.704318	0.704521	0.706213	0.704441	0.704429	0.704637	0.705568	0.705064	
2se	0.000010	0.000016	0.000022	0.000011	0.000025	0.000167	0.000011	0.000018	0.000020	0.000095	0.000188	
Sm ($\mu g \bullet g^{-1}$)	5.34	4.11	4.08	4.18	3.39	2.12	3.64	2.58	2.84	4.63	2.69	
Nd	24.4	19.0	15.2	19.6	17.8	14.5	18.2	13.1	14.9	23.3	18.7	
$^{143}Nd/^{144}Nd_m$	0.512774	0.512744	0.512769	0.512743	0.512719	0.512646	0.512740	0.512746	0.512738	0.512719	0.512670	0.512776
2se	0.000005	0.000007	0.000005	0.000006	0.000005	0.000004	0.000005	0.000004	0.000004	0.000004	0.000005	0.000004
$^{147}Sm/^{144}Nd$	0.1325	0.1308	0.1626	0.1295	0.1159	0.0887	0.1215	0.1191	0.1154	0.1203	0.0874	
$^{143}Nd/^{144}Nd_i$	0.512748	0.512718	0.512737	0.512716	0.512695	0.512627	0.512715	0.512721	0.512721	0.512701	0.512655	
2se	0.000006	0.000007	0.000006	0.000006	0.000006	0.000004	0.000005	0.000004	0.000004	0.000005	0.000005	
εNd_i	2.27	1.69	0.26	1.65	1.23	−0.09	1.62	1.74	1.74	1.36	0.45	
Pb ($\mu g \bullet g^{-1}$)	10	21	7	16	46	75	17	23	36	57	145	
U	1.63	2.57	1.05	2.57	5.63	44	1.75	2.19	5.89	9.97	102	
Th	5.57	8.23	3.80	7.47	17.1	153	6.79	11.3	20.5	34.0	285	
$^{206}Pb/^{204}Pb_m$	18.867	18.849	18.888	18.867	18.866	19.044	18.854	18.856	18.902	18.890	19.089	18.945
2se	0.006	0.006	0.006	0.006	0.006	0.006	0.006	0.006	0.007	0.006	0.006	0.006
$^{207}Pb/^{204}Pb_m$	15.640	15.629	15.643	15.638	15.651	15.655	15.630	15.624	15.648	15.653	15.657	15.661
2se	0.007	0.007	0.007	0.007	0.007	0.007	0.007	0.007	0.008	0.007	0.007	0.007
$^{208}Pb/^{204}Pb_m$	39.154	39.051	39.130	39.105	39.121	39.340	39.064	39.050	39.135	39.164	39.333	38.578
2se	0.023	0.024	0.023	0.024	0.024	0.024	0.024	0.024	0.025	0.024	0.024	0.023
$^{206}Pb/^{204}Pb_i$	18.817	18.826	18.843	18.815	18.827	18.850	18.820	18.825	18.864	18.850	18.896	
2se	0.006	0.006	0.007	0.006	0.006	0.007	0.006	0.006	0.007	0.006	0.009	
$^{207}Pb/^{204}Pb_i$	15.638	15.628	15.641	15.635	15.650	15.646	15.629	15.623	15.646	15.652	15.648	
2se	0.007	0.007	0.007	0.007	0.007	0.007	0.007	0.007	0.008	0.007	0.007	
$^{208}Pb/^{204}Pb_i$	39.098	39.012	39.076	39.055	39.082	39.118	39.022	38.998	39.092	39.119	39.155	
2se	0.023	0.024	0.024	0.024	0.024	0.024	0.024	0.024	0.025	0.024	0.025	

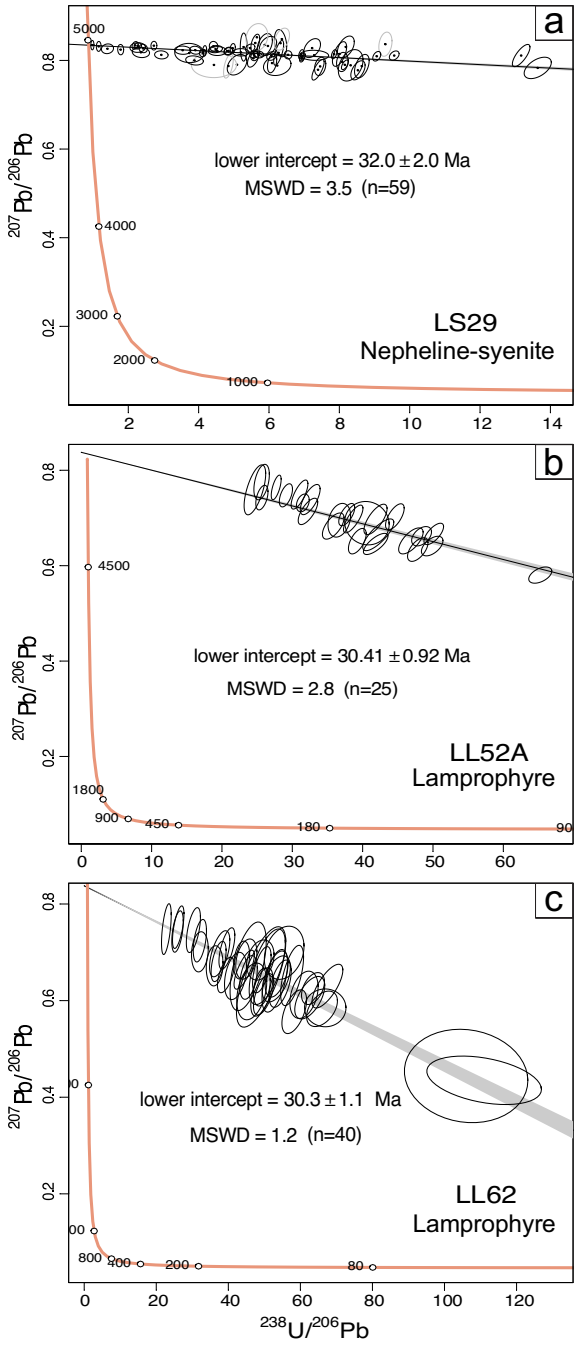

Fig. 10. U-Pb Discordia diagrams as obtained from the *in-situ* apatite dating from the studied magmatic rock samples.

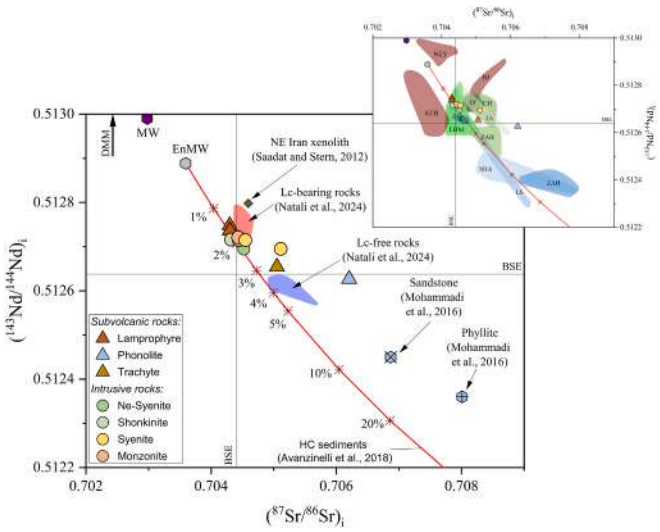

Fig. 11. Initial Sr-Nd isotope ratios of rocks from the Lar complex (SE Iran). EnMW is the composition of the mantle wedge (MW; Sr = 22 ppm, $^{87}Sr/^{86}Sr$ = 0.70298, Nd = 0.3 ppm, $^{143}Nd/^{144}Nd$ = 0.51299; Natali et al., 2024) after the first metasomatic events obtained by the addition of 6% of slab partial melts (Sr = 630 ppm, $^{87}Sr/^{86}Sr$ = 0.70393, Nd = 3.0 ppm, $^{143}Nd/^{144}Nd$ = 0.51273; Natali et al., 2024) of Kermanshah (Saccani et al., 2013) and Neyriz (Moghadam et al., 2014) ophiolites as AOC. The red mixing line represents the second metasomatic events characterized by the addition of high-carbonate (HC) sediment melts to the EnMW mantle source, respectively. The composition of AOC partial melts and those of HC (Apennine marlstone SD48 – Avanzinelli et al., 2018; Sr = 867 ppm, $^{87}Sr/^{86}Sr$ = 0.708040, Nd = 17.3 ppm, $^{143}Nd/^{144}Nd$ = 0.512163) sediments partial melts were obtained using bulk/melt ratios from the experimental work of Carter et al. (2015) for AOC, and Skora et al. (2015) for HC and LC, at temperatures between 900 and 1000 °C. Values for Bulk Silicate Earth (BSE) from Zindler and Hart (1986). The distribution of other igneous complexes along the Sistan Suture Zone is also shown in the inset for comparison, with blue fields representing Eocene-aged igneous complexes, green fields corresponding to Oligocene-aged ones, and brown fields indicating ophiolites. ZAH – Zahedan pluton (Mohammadi et al., 2016); LS – Lut-Sistan igneous complexes (Pang et al., 2013); Shah Kuh pluton (Mohammadi et al., 2016); CH – Chah-Shaljami granitoids (Arjmandzadeh et al., 2011a); D – Dehsalm granitoids (Arjmandzadeh and Santos, 2014); K – Koudakan intrusion (Omidianfar et al., 2020); LHM – Lar/Hormak/Malek Siah Kuh complexes (Sargazi et al., 2022); KER – Kermanshah ophiolite (Saccani et al., 2013); BJ – Birjand ophiolite (Zarrinkoub et al., 2012); NEY – Neyriz ophiolite (Moghadam et al., 2014); DMM – Depleted MORB Mantle (Workman and Hart, 2005). For interpretation of the references to colour in this figure legend, the reader is referred to the web version of this article.

complexes (Pang et al., 2013) – from the Sistan belt, although the Lar complex is characterized by the least radiogenic Sr values of the region only comparable to those found in the Koudakan intrusion (Omidianfar et al., 2020) in the Lut block.

The initial $^{206}Pb/^{204}Pb$, $^{207}Pb/^{204}Pb$ and $^{208}Pb/^{204}Pb$ values of the Lar rocks are relatively homogeneous, varying from 18.82 to 18.90, 15.62 to 15.65, and to 39.00 to 39.16, respectively (Fig. 12a-b). The $^{207}Pb/^{204}Pb_i$ and $^{208}Pb/^{204}Pb_i$ isotopic values of the investigated samples are distinctly higher than the Northern Hemisphere Reference Line (NHRL; Hart, 1984) and in the range of modern marine sediments (Ben Othman et al., 1989). Their Pb isotopic composition shows more radiogenic values than Eocene silica-undersaturated rocks from NW Iran (Natali et al., 2024; Fig. 12).

5. Discussion

5.1. Magmatic affinities and the evolution of Lar Igneous complex

The Lar Igneous Complex belongs to the Sefidabeh geologic complex of the SSZ, a geologic structure that marks the collision area between the Afghan and Lut continental blocks. Magmatic activity within the Sefidabeh geologic complex spans in age from late Cretaceous to early Oligocene, and it is associated with the emplacement of volcanic and intrusive rocks. The volcanic rocks range in composition from subduction-related calc-alkaline types to shoshonitic types, which formed during post-orogenic phases.

Based on petrographic and geochemical data, three main types of igneous suites, differing in both silica saturation and magmatic affinity, were recognized among the Lar rocks (Fig. 13): i) silica-oversaturated (monzonites), ii) silica-undersaturated (lamprophyres, phonolites and nepheline-syenites), and iii) silica-saturated rocks (syenites and trachytes). The occurrence of both silica-undersaturated and -oversaturated to saturated samples in the same igneous complex raises a

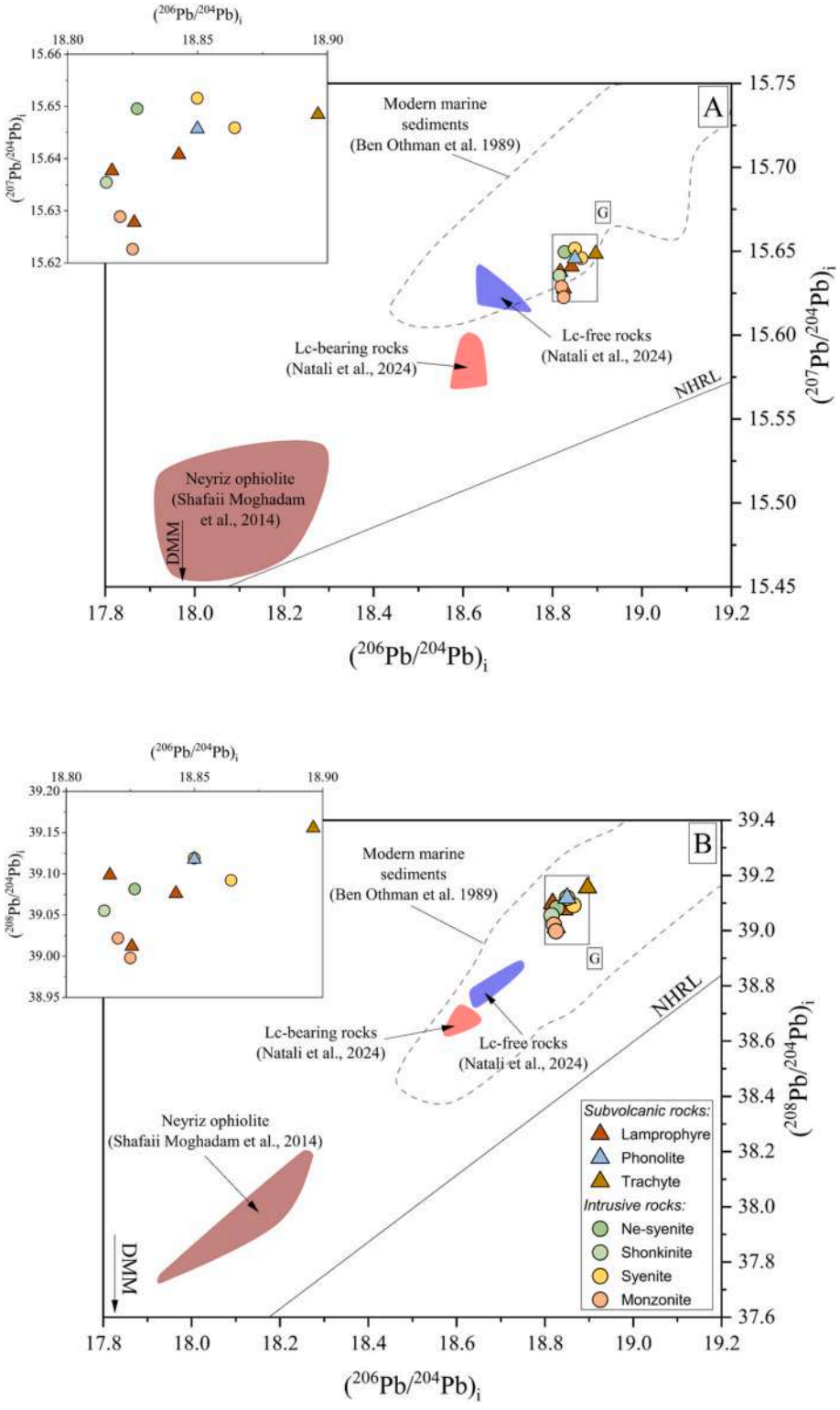

Fig. 12. Initial a) $^{207}Pb/^{204}Pb$ *vs* $^{206}Pb/^{204}Pb$ and b) $^{208}Pb/^{204}Pb$ *vs* $^{206}Pb/^{204}Pb$ isotope ratios of igneous rocks from the Lar Complex (SE Iran). The distribution of the leucite-free and leucite-bearing rocks from the Ahar-Arasbaran region (NW Iran) of Natali et al. (2024), as well as of the Neyriz ophiolite (SW Iran) of Moghadam et al. (2014), are also reported for comparison. Data of modern marine sediments are from Ben Othman et al. (1989). The Northern Hemisphere Reference Line (NHRL) is from Hart (1984). G = global subducting sediments (GLOSS; Plank and Langmuir, 1998); DMM = Depleted MORB Mantle (Workman and Hart, 2005).

question about their origin in the framework of the magmatic evolution in the Lut-Sistan region.

The chronological relationships among these three rock groups remain poorly constrained. The available age data from literature on Lar Igneous rocks indicate that plutonic monzonitic rocks were intruded between ~33 and 31 Ma, although a younger age of ~27 Ma was found using the K-Ar method on biotite separates (Camp and Griffis, 1982; Sargazi et al., 2022). The new geochronological data presented herein refine the emplacement age of the Lar igneous complex to the early Oligocene (in the time span 32–29 Ma), although a single early Miocene

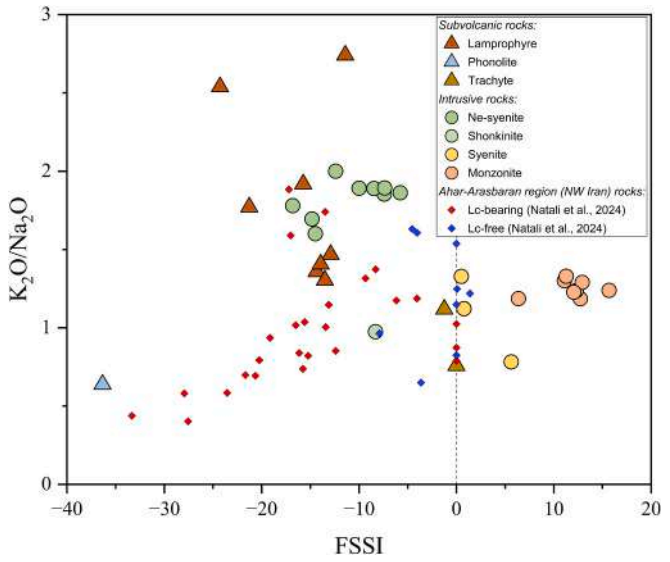

Fig. 13. Bivariate diagram comparing the degree of silica saturation (FSSI, Feldspathoid Silica Saturation Index; FSSI = Qz – Lc + 2(Ne + Kp)) and the K_2O/Na_2O ratio, showing the different silica-saturation conditions of Lar's igneous rocks. Qz – quartz; Lc – leucite; Ne – nepheline; Kp – kaliophillite.

age was obtained *via* K-Ar dating on a syenite sample. Although the analyzed zircons are typically strongly altered by intense fluid–rock interaction, with internal textures (Fig. S1) compatible with fluid-mediated alteration involving dissolution–reprecipitation processes (Booth et al., 2005; Geisler et al., 2007) and highly Th-rich compositions (up to 44,000 ppm Th with unusually high Th/U ratios), the analyses define coherent Discordia arrays (Fig. 9). High Th concentrations promote metamictization, leading the zircon susceptible to fluid-driven coupled dissolution–reprecipitation (Geisler et al., 2007; Kirkland et al., 2015). This fluid-mediated alteration ultimately reset the U-Pb isotopic clock within the altered domains (*e.g.*, Daczko et al., 2024; Geisler et al., 2007; Rubatto et al., 2008). Consequently, the altered domains exhibit a spread in U-Pb ratios, driving the analytical spots away from the Concordia curve and resulting in the observed systematic discordance (Fig. 9). However, this systematic discordance suggests that the intercept ages retain genuine geological significance rather than reflecting random analytical disturbance (Fig. 9). Significantly, the oldest ages are provided by U-Pb zircon data from the phonolite sample LD-3 (32.46 ± 0.38 Ma) and by whole rock K-Ar dating from the nepheline syenite LS-55 (32.2 ± 0.7 Ma), both overlapping within error with apatite U-Pb results from nepheline syenite LS-29 (32.0 ± 2.0 Ma, Figs. 9 and 10). Slightly younger ages are recorded by zircon U-Pb data on LM-11 (31.22 ± 0.38 Ma) and whole rock K-Ar age on LM-14 (31.1 ± 0.8 Ma) monzonite samples. Apatite U-Pb analyses provided similar ages at 30.41 ± 0.92 Ma and 30.3 ± 1.1 Ma for lamprophyres (minette) (samples LL-52A and LL-62) consistent with zircon U-Pb data from sample LL-62 (29.7 ± 1.1 Ma, Figs. 9 and 10). A slightly younger crystallization age is given by the trachyte sample LL-52B, which provided a zircon U-Pb age of 29.32 ± 0.61 Ma, whereas the youngest age of the suite (22.8 ± 0.7 Ma) was obtained by whole rock K-Ar analysis of the syenite LS-56 sample. Unfortunately, U-Pb ages were not available for this sample due to the lack of suitable mineral phases. Therefore, this early Miocene syenite K-Ar age was not considered in the following discussion.

Collectively, geochronological data confirm the early Oligocene timing of formation and emplacement of the Lar igneous complex (Camp and Griffis, 1982; Sargazi et al., 2022) and suggest that it incrementally developed through three main magmatic pulses. The oldest one is related to the almost coeval emplacement of the silica-undersaturated K-rich phonolitic dykes at 32.46 ± 0.38 and of the nepheline syenite pluton(s) between 32.2 ± 0.7 and 32.0 ± 2.0 Ma. The second magmatic pulse corresponds to the intrusion of the quartz-bearing monzonitic magma at 31.6 ± 0.38 Ma. The third magmatic pulse corresponds to the emplacement of lamprophyric dykes (minette) between 30.3 ± 1.1 and 29.7 ± 1.7 Ma, and the coeval subvolcanic silica-saturated trachytic dykes at 29.3 ± 0.6 Ma. This sequence indicates that the magmatic evolution of the Lar igneous complex was characterized, in its most differentiated lithotypes, by a decrease in alkalinity and an increase in silica saturation over time, from phonolites to trachytes and (possibly) from Ne-syenite to syenite. Silica-oversaturated rocks were restricted to an intermediate event plausibly involving crustal melting, consistent with what has been also reported in the literature (Camp and Griffis, 1982).

5.2. Magmatic differentiation

The major and trace element compositions of the rocks from the Lar igneous complex, together with their isotopic values, are used to identify the possible genetic relationships occurring among the different groups of rocks. A thermodynamically based fractional crystallization modelling was carried out to verify possible comagmatic relationships among the Lar lithotypes. Modelling was performed using the PELE software (Boudreau, 1999), assuming the lamprophyric samples as parental magmas, since they represent the only possible mafic lithotype of the sample set. The conditions of pressure, temperature and oxygen fugacity were derived from phase equilibria constraints reported in Ghafaribijar et al. (2019). The initial water content of lamprophyres was deduced from literature studies and by the modal amount of hydrated mineral phases identified through petrographic analysis. The modelled differentiation trends are reported in the R1-R2 diagram (De la Roche et al., 1980; Fig. 14). The lamprophyre sample LL-55 was selected as the starting composition, as it represents one of the most mafic samples and contains mafic minerals displaying textural features indicative of

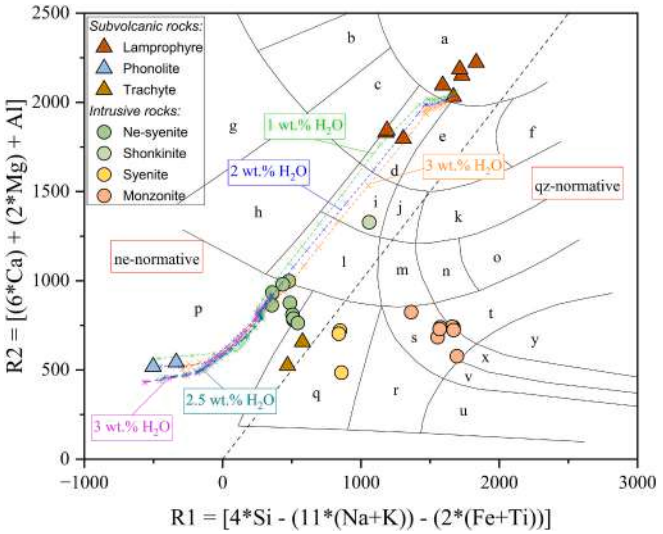

Fig. 14. R1-R2 [R1 = 4Si – 11(Na + K) – 2(Fe + Ti); R2 = 6Ca + 2 Mg + Al] classification diagram for the Lar's igneous rocks. Fractional crystallization paths calculated with PELE software (Boudreau, 1999) are also reported. Three different paths, with an H_2O content between 1 and 3 wt%, start from the lamprophyre (LL-55) and reach the composition of the nepheline syenites. Two additional paths, with an H_2O content of 2.5 and 3 wt%, start from the composition of the nepheline syenite (sample LS-55) and reach the composition of the phonolites. a – ultramafic rock; b – melteigite; c – theralite; d – alkali gabbro; e – gabbro; f – gabbro-norite; g – ijolite; h – essexite; i – syeno-gabbro; j – monzo-gabbro. k – gabbro-norite; l – syeno-diorite; m – monzonite; n – monzo-diorite; o – diorite; p – nepheline-syenite; q – syenite; r – quartz syenite; s – quartz monzonite; t – tonalite; u – alkali granite; v – syeno-granite; x – monzo-granite; y – granodiorite.

equilibrium. The modelled differentiation trend reproduces the compositional variation of nepheline-syenites through fractional crystallization of 23–24 vol% of olivine, 27–31 vol% of clinopyroxene, 5–7 vol% of spinel, and 1–1.5 vol% of apatite, as well as 0–0.3 vol% of leucite or 0.2–0.3 vol% of micas, depending on the assumed initial water content (1 and 2 wt%, respectively, green and blue dashed lines of Fig. 14). The modelled nepheline syenites represent 36–42 vol% residual fraction of the lamprophyric parent magma at a temperature of about 1000 °C.

Through the same modelling, the fractional crystallization path of the lamprophyric parent magma allows the reproduction of the compositional variation of the phonolites, by the crystallization of 32–33 vol% of clinopyroxene, ~24 vol% of olivine, 6–11 vol% of alkali-feldspar, 4–7 vol% of plagioclase, ~7 vol% of spinel, and ~ 1.5 vol% of apatite, as well as either ~5 vol% of leucite or ~ 0.3 vol% of biotite, depending on the assumed initial water content of the parental magma. The phonolites constitute 10–20 vol% residual fraction of the initial lamprophyre magma at a temperature of around 700 °C.

An increase in the initial water content of the magma (up to 3 wt%) still allows the compositional range of the nepheline syenites to be reproduced through fractional crystallization of the same amounts of olivine, clinopyroxene, spinel, and apatite as previously indicated, but with a higher proportion of biotite, reaching up to 2 vol% (orange line in Fig. 14). However, the higher water content makes it more difficult to model the evolution toward the phonolite compositional range, as it significantly favours biotite crystallization (from ~0.3 vol% to ~2 vol%) over alkali-feldspar (from 6 to 11 vol% to ~3 vol%) crystallization.

The model correctly predicts the crystallization of plagioclase in the second step of fractionation in agreement with the petrographic observations and with the distribution of rare earths that shows a clear negative anomaly in Eu (coupled with a negative anomaly in Sr) only in the most differentiated samples (Fig. 8). In addition, the initial crystallization temperature of biotite of about 1100 °C is higher than that reported in the study by Ghafaribijar et al. (2019), likely attributable to the fact that the analyses carried out by the authors were performed on a syenite sample, rather than on nepheline-syenites.

The geochemical compositional range of the phonolites can likewise be nearly reproduced starting from a magma composition comparable to that of nepheline syenite sample LS-55, through fractional crystallization of 5–6 vol% of olivine, 27–29 vol% of plagioclase, 3–15 vol% of alkali feldspar, 0–0.03 vol% of magnetite-ulvöspinel, ~2 vol% of leucite, 11–13 vol% of biotite, and ~ 2 vol% of apatite, assuming an initial H_2O content between ~2.5 and ~ 3 wt% (teal and bright magenta thick lines in Fig. 14). The modelled phonolites correspond to 34–48 vol% residual melt derived from the ne-syenite parent magma, at temperatures of approximately 700–750 °C. However, the modelled trend plots slightly below the measured phonolite compositions, likely due to the excessive crystallization of olivine, which results in a significant reduction in the R2 value.

The models also indicate that the composition of monzonites cannot be reproduced by fractional crystallization of lamprophyric magmas, precluding any possible comagmatic relationship between silica-undersaturated and -oversaturated rocks.

The REE distribution, in turn, shows distinct LREE/HREE fractionation among the recognized rock groups. In particular, the silica-undersaturated group of rocks shows the highest LREE/HREE (La_N/Yb_N from 11 to 15 for lamprophyres, from 18 to 22 for nepheline-syenites), whereas silica-oversaturated and -saturated group of rocks shares a lower La_N/Yb_N range (from 10 to 12 for monzonites and trachytes).

Summarizing, modelling results indicate that a genetic relationship, in terms of magmatic affinity, links the most silica-undersaturated products such as lamprophyres, nepheline syenites and phonolites. Silica-saturated (syenites and trachytes) and -oversaturated (monzonites) could instead represent differentiation products of distinct parental magmas not included in the studied sample suite.

5.3. Magma genesis and mantle sources of the Lar Igneous complex

Despite their different silica saturation degrees, Lar's rocks show similar Sr-Nd-Pb isotopic ratios (Fig. 11). This is particularly relevant for monzonites that, given their silica-oversaturated and peraluminous character could be interpreted as product of crustal anatexis possibly triggered by underplating of mafic magmas (*e.g.*, Visonà et al., 2025). Such a process however would result in invariably low $^{143}Nd/^{144}Nd$ values, which is in contrast with what observed. Only three samples (syenite LS-56, trachyte LL-52B and phonolite LD-3) are characterized by markedly higher radiogenic Sr composition, suggesting that they could have been affected by a crustal contamination/assimilation process (Fig. 11). In all the other samples crustal contamination plays a minor role. Indeed, the Sr isotopic ratio does not show significant variation along with the 1.17–16.02 wt% MgO range (LM-14 and LL-31, respectively), increasing only in the samples with lower MgO (< 0.22 wt %). This can also be verified using isotopic ratios and geochemical markers as relationships between elements that are very different between magmatic rocks and the continental crust. In fact, the variation of ($^{87}Sr/^{86}Sr$) with Rb/Sr (Fig. S2) and Nb/La (Fig. S3) indicates that only the most differentiated terms are variably affected by a process of assimilation coupled with fractional crystallization (AFC).

Overall, the incompatible elements distribution displays ubiquitous negative anomaly in Nb, Ta and Ti and positive anomalies in Pb (Fig.8a-e), indicating for the whole sample set a derivation from a common subduction-related mantle source (*e.g.*, Elliott, 2003).

The geochemical and mineralogical components of the source(s), which originated the observed magma types, were highlighted by considering only the least evolved terms (lamprophyres, Mg# > 67), as they represent the magmatic products more akin to primary mantle melts. In fact, lamprophyres in orogenic contexts are generally characterized by high potassium content, low degree of evolution (high Cr and Ni, high Mg# up to 79), and high LILE content. These geochemical features are indicators of the partial melting of the rock constituting the lithospheric mantle wedge metasomatized by fluids/melts from the subducted slab (*e.g.*, Conticelli et al., 2009). Hydrated silicate fluids (and/or melts) can be released from the subducted slab and cause metasomatism in the overlying mantle wedge (*e.g.*, Avanzinelli et al., 2009, 2012; Elliott, 2003). At medium-low pressures the dominant hydrated phases in the subducting crust consist of amphibole, biotite, muscovite and epidote. These minerals, however, become unstable under high pressure conditions, where phengite becomes the main stable phase. In fact, recycled continental rocks subducted beyond 100 km depth present a uniform metamorphic paragenesis composed of, in order of abundance, garnet, clinopyroxene, phengite, coesite, cyanite, and rutile in variable proportions (*e.g.*, Hermann and Green, 2001; Schmidt et al., 2004; Schmidt and Poli, 1998). The recycling of crustal components within the mantle usually occurs in the form of melts and/or fluids derived from subducted sediments and/or continental rocks (*e.g.*, Avanzinelli et al., 2009, 2012; Elliott, 2003).

At pressures of 3–4 GPa, partial melting caused by saturation in fluids (dehydration melting) occurs around 700–800 °C, while under anhydrous conditions it occurs at about 900–1000 °C. The melts are characterized by high K/Na values, given by the contribution of the hydrated phases (phengite or phlogopite) and by the retention of Na in jadeite, which is stable in those P-T conditions (Schmidt et al., 2004). Modal metasomatism in the mantle wedge includes, in addition to orthopyroxene, clinopyroxene and garnet, hydrated phases such as phlogopite and/or richterite-pargasite (Rapp et al., 1999).

According to Furman and Graham (1999), melts generated by an amphibole-bearing source, where Rb, Sr and Ba are moderately compatible, have Rb/Sr values less than 0.1 and Ba/Rb values greater than 20. On the contrary a phlogopite-bearing mantle source would be enriched in Rb, generating melts with high Rb/Sr and low Ba/Rb values (LaTourrette et al., 1995). These characteristics are also reported in a study on the chemistry of the mineral phases in mantle xenoliths (Ionov

and Hofmann, 1995), where it was observed that amphibole is characterized by high K and low Rb, while phlogopite is rich in both K and Rb. Therefore, the geochemical signature of the phlogopite contribution to the magma genesis would be precisely a high potassium content and a high Rb/Sr value in the samples (Fig. 15). Rocks of the Lar igneous complex have Rb/Sr values ranging between 0.06 and 0.19 and of Ba/Rb values between 8.21 and 18.7, attesting the predominance of the phlogopite contribution in the mantle source, in agreement with results presented by Sargazi et al. (2022). Moreover, the elemental ratios of the Lar rocks are consistent with those of potassic to ultrapotassic rocks from various Mediterranean magmatic provinces (Casalini et al., 2022; Tommasini et al., 2011), which are derived from a phlogopite-bearing mantle source (*e.g.*, Ammannati et al., 2015; Condamine and Médard, 2014; Förster et al., 2019; Prelević et al., 2008).

As previously presented, the Sr-Nd-Pb isotopic composition of the Lar igneous rocks is quite uniform clustering around that of a mantle xenolith from the NE Iran, which reflects the suprasubduction metasomatized mantle underlying the SSZ (Saadat and Stern, 2012). The Lar igneous rocks are isotopically comparable to those of other Oligocene subduction-related alkaline igneous complexes in the Lut-Sistan sector (green fields in the inset of Fig. 11), suggesting that a similar metasomatism affected the underlying mantle all along this area. Their composition, characterized by relatively unradiogenic Sr and radiogenic Nd, suggests a relatively small role of the sedimentary component in the generation of the metasomatic agent. The relatively homogenous isotope composition of silica-undersaturated, −saturated, and -oversaturated magmas suggests that they share a similar mantle source that was affected by different melting events over time along the mantle section. This rise the petrological issue of the coexistence of both silica-undersaturated and -oversaturated magmas that appear to be produced by the same mantle source. Geochronological results indicate indeed that both the silica-undersaturated (lamprophyre-Ne-syenite-phonolite)

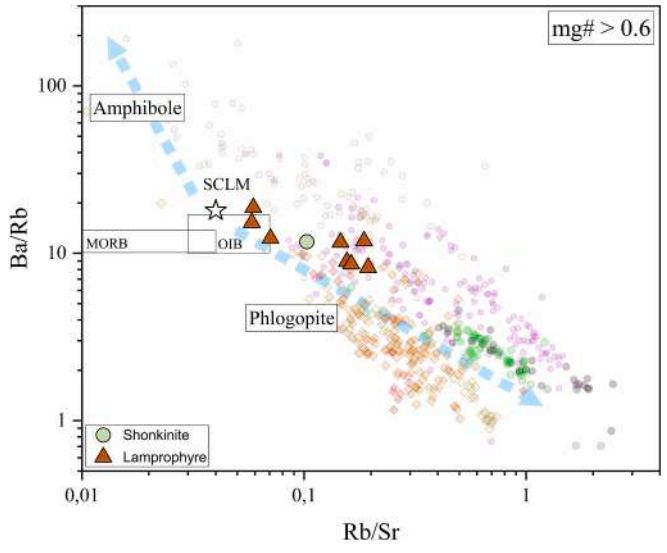

Fig. 15. Rb/Sr *vs.* Ba/Rb bivariate diagram showing only Lar samples with Mg# > 0.6. The compositional range of the Lar rocks highlights a predominant phlogopite contribution in the mantle source. Violet circles represent Tethyan Realm lamproites, whereas orange circles indicate within-plate lamproites (Tommasini et al., 2011, and references therein). Additional comparative samples are from Conticelli et al. (2015) and references therein) and correspond to magmatic rocks from Corsica and from the Tuscan and Roman magmatic provinces (symbols as in the original work). The composition of the Subcontinental Lithospheric Mantle (SCLM; McDonough, 1990) is shown together with qualitative arrows illustrating the expected compositional variations resulting from amphibole- *versus* phlogopite-driven mantle metasomatism. (For interpretation of the references to colour in this figure legend, the reader is referred to the web version of this article.)

and the silica-oversaturated (monzonite) suites were produced by the first melting event (corresponding to the emplaced magmas at ~32 Ma), whereas the second melting event generated the silica-saturated trachytes at *ca.* 29 Ma.

The dichotomy in silica saturation among the Lar igneous rocks is associated with i) field observation showing that all these rocks coexist in a restricted area (~36 km^2) with sharp contacts (Sargazi et al., 2022); ii) their closely related emplacement ages; and iii) their similar Sr-Nd-Pb isotopic composition, collectively suggesting small-scale heterogeneity within the mantle beneath the Lar area. The genesis of ultrapotassic silica-undersaturated magmas requires high XCO_2 conditions in the mantle source, which can be provided by a carbonated subducted component. In other sectors of the Alpine-Himalayan belt the coexistence of both silica-undersaturated and -oversaturated magmas has been explained by recycling of carbonate-rich and -poor sediments, respectively (Avanzinelli et al., 2008, 2009; Conticelli et al., 2015). Alternatively, a recent experimental study of Gülmez et al. (2023) demonstrated that partial melting of carbonate-rich siliciclastic sediments (carbonaceous pelite) can generate two conjugate melts: i) a carbonate melt and ii) a highly K-enriched silicate melt. These two liquids are completely immiscible, forming distinct domains that interact separately with the mantle mineral assemblage. The mineral assemblage formed within the carbonate domains—wherlitic peridotite containing phlogopite, amphibole, and carbonate minerals/glass—closely resembles the compositions proposed for the mantle sources of orogenic, silica-undersaturated magmas (*e.g.*, Ammannati et al., 2015; Bonadiman et al., 2021). In contrast, the more silicate-rich metasomatic agent would produce orthopyroxene-rich mantle domains also containing phlogopite that can give rise to silica-oversaturated rocks (Avanzinelli et al., 2020; Dallai et al., 2019, 2022).

In order to explain the complex metasomatic processes that contributed to the geochemical and isotopic composition of Lar magmas a two-step mass balance model was developed, considering the interplay between a the pre-metasomatism mantle wedge and partial melts/supercritical fluids from i) the altered oceanic crust (AOC) and ii) different types of subducted sediments. The pre-metasomatized mantle wedge and the AOC composition have been calculated based on the least metasomatized or altered mafic rocks from ophiolites of the Neo-Tethys as they represent the most reliable evidence of subducted basaltic crust (Neyriz ophiolite, Moghadam et al., 2014; Kermanshah ophiolite, Saccani et al., 2013). The composition of the AOC-derived component was obtained by the application of experimental results of Carter et al. (2015) at 3 GPa and temperature between 900 and 1000 °C (for partial melts) and of Kessel et al. (2005) at 4 GPa and temperature between 900 and 1000 °C (for supercritical fluids) to the average local ophiolites. As sedimentary components we first tested the locally obducted siliciclastic sediments, consisting of a phyllite and a sandstone from the Sistan Flysch (Mohammadi et al., 2016). The composition of the sediment partial melts was calculated using the experimental results of Skora et al. (2015), performed at 3 GPa and 900–1000 °C.

The resulting geochemical and isotopic mass balance model using these local Si-rich flyschoid lithologies (Figs. S4 and S5) and the metasomatized mantle by the altered oceanic crust failed to reproduce the Lar's rock compositions (and other nearby complexes). The model results suggest that a sedimentary component with comparatively higher Sr/Nd values and different isotopic signature is needed to reproduce the data, which can be plausibly represented by carbonate-rich sediments. A possible contribution of carbonate-rich sediments to the geochemical signature of the Lar magmas is also supported by the similarity between their isotopic compositions with those of the most undersaturated leucite-bearing lavas studied by Natali et al. (Natali et al., 2024; Fig. 11), whose genesis has been attributed to the addition of a small amount of partial melts from high-carbonate (HC) sediments to the enriched mantle wedge.

Due to the lack of available data on local, carbonate-rich, obducted lithologies, we performed the model using sedimentary rocks from other

sectors of the Alpine–Himalayan domains related to the Tethys closure. The potential uncertainties associated with this assumption are reasonable, since these rocks formed in the same regional tectonic context. In particular, we tested carbonate-poor (Fig. S6), and -rich (Fig. 11) marlstones from the Northern Apennines (Avanzinelli et al., 2018; Conticelli et al., 2002, 2015), as well as a high-carbonate (Ca wt% up to 10) sandstone sample from Serbian flysch (Fig. S7, Prelević et al., 2008). Similarly to the local lithologies, the carbonate-poor marlstone also fails to account for the isotopic composition of the Lar rocks (Fig. S6). In contrast, the isotopic composition of the Lar's rocks can be reproduced either by i) the addition of 1–3% of carbonate-rich marlstone melts (Fig. 11), or ii) 2–4% of carbonate-rich sandstone melt (Fig. S7). This is due to the distinct trends generated by the differing Sr/Nd ratios of the metasomatic agents, being too low for both the local Si-rich sediment melts and the carbonate-poor marl melts.

The proposed model explains all the variability observed in the orogenic-affinity alkaline complexes of the Sistan-Lut region, through the varying contributions of the end-members considered above (namely the high-carbonate marlstone and the high carbonate sandstone). Igneous rocks from the several other complexes within the Lut–Sistan region highlight a temporal isotopic shift, with Eocene complexes showing more radiogenic Sr and less radiogenic Nd compositions compared to the Oligocene ones (Fig. 11). Within this general trend, the Lar igneous rocks display the least radiogenic Sr and the most radiogenic Nd values of the isotopic range defined by the Oligocene subduction-related alkaline complexes of the Lut–Sistan sector. This is compatible with the hypothesis of a decrease of the metasomatic contribution (of sedimentary origin) to the magma sources from Eocene to Oligocene times (*e.g.*, Mohammadi et al., 2016; Pang et al., 2013; Sargazi et al., 2022).

5.4. Geodynamic synthesis

The final closure of the Sistan Ocean, leading to the collision between the Lut and Afghan blocks, likely initiated during the Late Cretaceous, as indicated by the emplacement of adakitic plutons derived from partial melting of a thickened lower crust (Jung et al., 1984; Zarrinkoub et al., 2012). The magmatic hiatus from the early Paleocene to the middle Eocene suggests a tectonic transition from compression to extension (Pang et al., 2013). Regional uplift and deposition of continental red beds interlayered with evaporites during this period further attest to crustal stabilization and lithospheric thickening along the southern Eurasian margin (Bagheri and Damani Gol, 2020; Tirrul et al., 1983).

From the middle Eocene to late Oligocene (~46–25 Ma), renewed magmatism affected the Lut–Sistan region, marking a post-collisional phase characterized by continuous mantle melting and crustal interaction (Omidianfar et al., 2023; Pang et al., 2013). The Lar complex, emplaced during the late stages of this post-collisional activity (~32–29 Ma), exhibits enrichments in LILE and Pb, coupled with Nb, Ta, and Ti depletions, signatures typical of subduction-related orogenic magmas. Isotopic and geochemical data indicate that these magmas were derived from partial melting of a phlogopite-bearing, subduction-modified lithospheric mantle, becoming progressively less influenced by sediment-derived metasomatism from the Eocene to the Oligocene (Fig. 11; Pang et al., 2013; Mohammadi et al., 2016; Sargazi et al., 2022).

Coherently with previous reconstructions, the Oligocene Lar magmatism can be framed within a scenario of gravitational instability and convective removal of the thickened lithospheric root formed after collision (Pang et al., 2013; Zarrinkoub et al., 2012). Delamination and subsequent asthenospheric upwelling triggered melting in the metasomatized mantle and established a subduction-modified asthenospheric window beneath the region. The infiltration of a younger, heterogeneous asthenosphere into shallower levels promoted mixing with carbonate-rich mantle domains, enhancing melt generation and producing the potassic to shoshonitic magmatism observed in the Lar complex.

To conclude, the Lar magmatism marks the final stage of a multiphase geodynamic evolution along the eastern Iranian orogenic belt. This evolution reflects the progressive transition from compression to extension, from Late Cretaceous subduction and crustal thickening, through Eocene to Oligocene post-collisional extension driven by lithosphere delamination and mantle upwelling.

6. Conclusions

The principal conclusions of this study are summarized as follows:

(i) The intrusive and hypabyssal rocks of the Oligocene Lar igneous complex are characterized by common subduction-related geochemical fingerprints, but very different degrees of silica saturation, including silica-undersaturated lamprophyres, nesyenites and phonolites, silica-saturated trachytes and syenites and silica-oversaturated monzonites.

(ii) Geochronological data indicate that these magmatic rocks were emplaced between *ca.* 32 and 29 Ma through three main magmatic pulses, without a clear magmatic evolution.

(iii) Geochemical and isotopic data indicate that the silica-undersaturated and -oversaturated magmatic rocks formed by melting of different mantle domains generated by carbonate-rich and -poor metasomatic agents that likely originate as conjugate liquids from calc-silicate subducted sediments (Gülmez et al. (2023).

Melting of these heterogeneous mantle domains was likely induced by asthenospheric mantle upwelling during post-collisional extension that succeeded the compressional stage(s) related to closure of the Sistan Ocean and collision between the Lut and Afghan continental blocks.

Supplementary data to this article can be found online at https://doi.org/10.1016/j.lithos.2026.108681.

CRediT authorship contribution statement

M. Ghiotto: Writing – original draft, Software, Methodology, Investigation, Formal analysis, Data curation, Conceptualization. **C. Natali:** Writing – original draft, Supervision, Software, Formal analysis, Data curation, Conceptualization. **A. Rabiee:** Writing – original draft, Software, Methodology, Formal analysis, Data curation. **A. Bragagni:** Writing – original draft, Software, Methodology, Formal analysis. **E. Braschi:** Software, Methodology, Data curation. **R. Avanzinelli:** Writing – original draft, Software, Methodology, Formal analysis, Data curation. **M. Casalini:** Software, Methodology, Formal analysis, Data curation. **S. Ghafaribijar:** Methodology, Investigation, Conceptualization. **M. Arvin:** Methodology, Investigation, Conceptualization. **F. Rossetti:** Writing – original draft, Methodology, Formal analysis, Data curation. **S. Conticelli:** Writing – original draft, Supervision, Investigation, Formal analysis, Data curation, Conceptualization.

Declaration of competing interest

The corresponding authors, on behalf of all the authors, declare no competing interest and that no AI technologies were used to prepare the submitted manuscript.

Acknowledgements

The authors thank the Editor and two anonymous reviewers for their constructive comments that allowed improving the submitted manuscript. The authors also thanks Dr. Chiara Maccelli for the analytical support in isotope analyses performed at the Laboratories “Filippo Olmi” of the Department of Earth Sciences of the University of Florence. This study was supported by ex-60% grants of the University of Florence

issued to C. Natali and M. Casalini and by the MUR-PRIN 2022 grant 2022PC9NME ("TRANSIENT"), awarded to Martina Casalini.

References

Agard, P., Omrani, J., Jolivet, L., Whitechurch, H., Vrielynck, B., Spakman, W., Monié, P., Meyer, B., Wortel, R., 2011. Zagros orogeny: a subduction-dominated process. Geol. Mag. 148, 692–725. https://doi.org/10.1017/S001675681100046X.

Ammannati, E., Jacob, D.E., Avanzinelli, R., Foley, S.F., Conticelli, C., 2015. Low Ni olivine in silica-undersaturated ultrapotassic igneous rocks as evidence for carbonate metasomatism in the mantle. Earth Planet. Sci. Lett. 444, 64–74. https://doi.org/10.1016/j.epsl.2016.03.039.

Arjmandzadeh, R., Santos, J., 2014. Sr-Nd isotope geochemistry and tectonomagmatic setting of the Dehsalm Cu-Mo porphyry mineralizing intrusives from Lut Block, eastern Iran. Int. J. Earth Sci. 103, 123–140.

Arjmandzadeh, R., Karimpour, M., Mazaheri, S., Santos, J., Medina, J., Homam, S., 2011a. Two-sided asymmetric subduction; implications for tectonomagmatic and metallogenic evolution of the Lut Block, eastern Iran. J. Econ. Geol. 3, 1–14. https://doi.org/10.22067/econg.v3i1.11445.

Arjmandzadeh, R., Karimpour, M., Mazaheri, S., Santos, J., Medina, J., Homam, S., 2011b. Sr-Nd isotope geochemistry and petrogenesis of the Chah-Shaljami granitoids (Lut Block, Eastern Iran). J. Asian Earth Sci. 41, 283–296. https://doi.org/10.1016/j.jseaes.2011.02.014.

Avanzinelli, R., Boari, E., Conticelli, S., Francalanci, L., Guarnieri, L., Perini, G., Petrone, C., Tommasini, S., Ulivi, M., 2005. High precision Sr, Nd, and Pb isotopic analyses using the new generation thermal ionisation mass spectrometer ThermoFinnigan Triton-Ti®. Periodico di Mineralogia 74, 147–166.

Avanzinelli, R., Elliott, T., Tommasini, S., Conticelli, S., 2008. Constraints on the genesis of potassium-rich Italian volcanic rocks from U/Th disequilibrium. J. Petrol. 49, 195–223. https://doi.org/10.1093/petrology/egm076.

Avanzinelli, R., Lustrino, M., Mattei, M., Melluso, L., Conticelli, S., 2009. Potassic and ultrapotassic magmatism in the circum-Tyrrhenian region: significance of carbonated pelitic vs. pelitic sediment recycling at destructive plate margins. Lithos 113, 213–227. https://doi.org/10.1016/j.lithos.2009.03.029.

Avanzinelli, R., Prytulak, J., Skora, S., Heumann, A., Koetsier, G., Elliott, T., 2012. Combined 238U-230Th and 235U–231Pa constraints on the transport of slab-derived material beneath the Mariana Islands. Geochim. Cosmochim. Acta 92, 308–328. https://doi.org/10.1016/j.gca.2012.06.020.

Avanzinelli, R., Casalini, M., Elliott, T., Conticelli, S., 2018. Carbon fluxes from subducted carbonates revealed by uranium excess at Mount Vesuvius, Italy. Geology 46, 259–262. https://doi.org/10.1130/G39766.1.

Avanzinelli, R., Bianchini, G., Tiepolo, M., Jasim, A., Natali, C., Braschi, E., Dallai, L., Beccaluva, L., Conticelli, S., 2020. Subduction-related hybridization of the lithospheric mantle revealed by trace element and Sr-Nd-Pb isotopic data in composite xenoliths from Tallante (Betic Cordillera, Spain). Lithos 352-353, 105316. https://doi.org/10.1016/j.lithos.2019.105316.

Bagheri, S., Damani Gol, S.D., 2020. The eastern Iranian orocline. Earth-Sci. Rev. 210, 103322. https://doi.org/10.1016/j.earscirev.2020.103322.

Beccaluva, L., Bianchini, G., Bonadiman, C., Siena, F., Vaccaro, C., 2004. Coexisting anorogenic and subduction-related metasomatism in mantle xenoliths from the Betic Cordillera (southern Spain). Lithos 75 (1–2), 67–87. https://doi.org/10.1016/j.lithos.2003.12.015.

Ben Othman, D., White, W.M., Patchett, J., 1989. The geochemistry of marine sediments, island arc magma genesis and crust-mantle recycling. Earth Planet. Sci. Lett. 94 (36), 912. https://doi.org/10.1016/0012-821X(89)90079-4.

Berberian, M., King, G., 1981. Towards a Paleogeography and Tectonic Evolution of Iran. Can. J. Earth Sci. 18, 210–265. https://doi.org/10.1139/e81-019.

Besse, J., Torcq, F., Gallet, Y., Ricou, L.E., Krystyn, L., Saidi, A., 1998. Late Permian to late Triassic palaeomagnetic data from Iran: constraints on the migration of the Iranian block through the Tethyan Ocean and initial destruction of Pangaea. Geophys. J. Int. 135, 77–92. https://doi.org/10.1046/j.1365-246X.1998.00603.x.

Bianchini, G., Beccaluva, L., Nowell, G., Pearson, D., Siena, F., 2011. Mantle xenoliths from Tallante (Betic Cordillera): insights into the multi-stage evolution of the south Iberian lithosphere. Lithos 124, 308–318. https://doi.org/10.1016/j.lithos.2010.12.004.

Bonadiman, C., Brombin, V., Andreozzi, G.B., Benna, P., Coltorti, M., Curetti, N., Faccini, B., Merli, M., Pelorosso, B., Stagno, V., 2021. Phlogopite-pargasite coexistence in an oxygen reduced spinel-peridotite ambient. Sci. Rep. 11, 11829. https://doi.org/10.1038/s41598-021-90844-w.

Bonnet, G., Agard, P., Angiboust, S., Moni'e, P., Jentzer, M., Omrani, J., Whitechurch, H., Fournier, M., 2018. Tectonic slicing and mixing processes along the subduction interface: the Sistan example (Eastern Iran). Lithos 310–311, 269–287. https://doi.org/10.1016/j.lithos.2018.04.016.

Boomeri, M., Moradi, R., Stein, H., Bagheri, S., 2019. Geology, Re-Os age, S and O isotopic composition of the Lar porphyry Cu-Mo deposit, Southeast Iran. Ore Geol. Rev. 104, 477–494. https://doi.org/10.1016/j.oregeorev.2018.11.018.

Boomeri, M., Moradi, R., Bagheri, S., 2020. Petrology and origin of the Lar igneous complex of the Sistan suture zone, Iran. Geologos 26, 51–64. https://doi.org/10.2478/logos-2020-0004.

Booth, A.L., Kolodny, Y., Chamberlain, C.P., McWilliams, M., Schmitt, A.K., Wooden, J., 2005. Oxygen isotopic composition and U-Pb discordance in zircon. Geochim. Cosmochim. Acta 69, 4895–4905. https://doi.org/10.1016/j.gca.2005.05.013.

Boudreau, A.E., 1999. PELE—a version of the MELTS software program for the PC platform. Comput. Geosci. 25, 201–203. https://doi.org/10.1016/S0098-3004(98)00117-4.

Bröcker, M., Hövelkröger, Y., Fotoohi Rad, G., Berndt, J., Scherer, E.E., Kurzawa, T., Moslempour, M.E., 2022. The magmatic and tectono-metamorphic history of the Sistan suture zone, Iran: new insights into a key region for the convergence between the Lut and Afghan blocks. J. Asian Earth Sci. 236, 105313. https://doi.org/10.1016/j.jseaes.2022.105313.

Camp, V., Griffis, R., 1982. Character, genesis and tectonic setting of igneous rocks in the Sistan suture zone, eastern Iran. Lithos 15, 221–239. https://doi.org/10.1016/0024-4937(82)90014-7.

Carter, A., Najman, Y., Bahroudi, A., Bown, P., Garzanti, E., Lawrence, R.D., 2010. Locating earliest records of orogenesis in western Himalaya: evidence from Paleogene sediments in the Iranian Makran region and Pakistan Katawaz basin. Geology 38, 807–810. https://doi.org/10.1130/G31087.1.

Carter, L.B., Skora, S., Blundy, J.D., de Hoog, J.C.M., Elliott, T., 2015. An experimental study of trace element fluxes from subducted Oceanic Crust. J. Petrol. 56, 1585–1606. https://doi.org/10.1093/petrology/egv046.

Casalini, M., Avanzinelli, R., Tommasini, S., Natali, C., Bianchini, G., Prelevic, D., Mattei, M., Conticelli, S., 2022. Petrogenesis of Mediterranean lamproites and associated rocks: the role of overprinted metasomatic events in the post-collisional lithospheric upper mantle. Geol. Soc. Lond. Spec. Publ. 513, 271–296. https://doi.org/10.1144/SP513-2021-36.

Chew, D.M., Petrus, J.A., Kamber, B.S., 2014. U–Pb LA–ICPMS dating using accessory mineral standards with variable common Pb. Chem. Geol. 363, 185–199. https://doi.org/10.1016/j.chemgeo.2013.11.006.

Condamine, P., Médard, E., 2014. Experimental melting of phlogopite-bearing mantle at 1 GPa: implications for potassic magmatism. Earth Planet. Sci. Lett. 397, 80–92. https://doi.org/10.1016/j.epsl.2014.04.027.

Conticelli, S., D'Antonio, M., Pinarelli, L., Civetta, L., 2002. Source contamination and mantle heterogenity in the genesis of Italian potassic and ultrapotassic volcanic rocks: Sr–Nd–Pb isotope data from Roman Province and Southern Tuscany. Mineral. Petrol. 74, 189–222. https://doi.org/10.1007/s007100200004.

Conticelli, S., Guarnieri, L., Farinelli, A., Mattei, M., Avanzinelli, R., Bianchini, G., Boari, E., Tommasini, S., Tiepolo, M., Prelévic, D., Venturelli, G., 2009. Trace elements and Sr–Nd–Pb isotopes of K-rich to shoshonitic, and calc-alkalic magmatism of the Western Mediterranean region: genesis of ultrapotassic to calc-alkaline magmatic associations in a post-collisional geodynamic setting. Lithos 107, 68–92. https://doi.org/10.1016/j.lithos.2008.07.016.

Conticelli, S., Laurenzi, M.A., Giordano, G., Mattei, M., Avanzinelli, R., Melluso, L., Tommasini, S., Boari, E., Cifelli, F., Perini, G., 2010. Leucite-bearing (kamafugitic/leucititic) and -free (lamproitic) ultrapotassic rocks and associated shoshonites from Italy: constraints on petrogenesis and geodynamics. In: Beltrando, M., Peccerillo, A., Mattei, M., Conticelli, S., Doglioni, C. (Eds.), J. Virtual Explor, 36. https://doi.org/10.3809/jvirtex.2009.00251 (paper 20).

Conticelli, S., Avanzinelli, R., Ammannati, E., Casalini, M., 2015. The role of carbon from recycled sediments in the origin of ultrapotassic igneous rocks in the Central Mediterranean. Lithos 232, 174–196. https://doi.org/10.1016/j.lithos.2015.07.002.

Daczko, N.R., Elliott, V., Piazolo, S., Hao, K., 2024. Zircon coupled dissolution–precipitation replacement during melt–rock interaction modifies chemical signatures resulting in misleading ages. J. Metamorph. Geol. 42, 1197–1214. https://doi.org/10.1111/jmg.12796.

Dallai, L., Bianchini, G., Avanzinelli, R., Natali, C., Conticelli, S., 2019. Heavy oxygen recycled into the lithospheric mantle. Sci. Rep. 9, 8793. https://doi.org/10.1038/s41598-019-45031-3.

Dallai, L., Bianchini, G., Avanzinelli, R., Deloule, E., Natali, C., Gaeta, M., Cavallo, A., Conticelli, S., 2022. Quartz-bearing rhyolitic melts in the Earth's mantle. Nat. Commun. 13, 7765. https://doi.org/10.1038/s41467-022-35382-3.

De la Roche, H., Leterrier, J., Grandclaude, P., Marchal, M., 1980. A classification of volcanic and plutonic rocks using R1R2-diagram and major-element analyses — its relationships with current nomenclature. Chem. Geol. 29, 183–210. https://doi.org/10.1016/0009-2541(80)90020-0.

Delavari, M., Amini, S., Schmitt, A.K., McKeegan, K.D., Harrison, T.M., 2014. U–Pb geochronology and geochemistry of Bibi-Maryam pluton, eastern Iran: implication for the late stage of the tectonic evolution of the Sistan Ocean. Lithos 200-201, 197–211. https://doi.org/10.1016/j.lithos.2014.04.015.

Dilek, Y., Imamverdiyev, N., Altunkaynak, Ş., 2010. Geochemistry and tectonics of Cenozoic volcanism in the Lesser Caucasus (Azerbaijan) and the peri-Arabian region: collision-induced mantle dynamics and its magmatic fingerprint. Int. Geol. Rev. 52, 536–578. https://doi.org/10.1080/00206810903360422.

Edgar, A.D., 1987. The genesis of alkaline magmas with emphasis on their source regions: inferences from experimental studies. Geol. Soc. Lond. Spec. Publ. 30, 29–52. https://doi.org/10.1144/GSL.SP.1987.030.01.04.

Elliott, T., 2003. Tracers of the slab. In: Eiler, J. (Ed.), Inside the Subduction Factory. Geophysical Monography, 138. American Geophysical Union, pp. 23–45.

Foley, S., 1992a. Petrological characterization of the source components of potassic magmas: geochemical and experimental constraints. Lithos 28, 187–204. https://doi.org/10.1016/0024-4937(92)90006-K.

Foley, S., 1992b. Vein-plus-wall-rock melting mechanisms in the lithosphere and the origin of potassic alkaline magmas. Lithos 28, 435–453. https://doi.org/10.1016/0024-4937(92)90018-T.

Förster, M.W., Prelević, D., Buhre, S., Mertz-Kraus, R., Foley, S.F., 2019. An experimental study of the role of partial melts of sediments versus mantle melts in the sources of potassic magmatism. J. Asian Earth Sci. 177, 76–88. https://doi.org/10.1016/j.jseaes.2019.03.014.

Furman, T., Graham, D., 1999. Erosion of lithospheric mantle beneath the East African Rift System: geochemical evidence from the Kivu Volcanic Province. Lithos 48, 237–262. https://doi.org/10.1016/S0024-4937(99)00031-6.

Geisler, T., Schaltegger, U., Tomaschek, F., 2007. Re-equilibration of zircon in aqueous fluids and melts. Elements 3, 43–50. https://doi.org/10.2113/gselements.3.1.43.
Ghafaribijar, S., Hakimi, J., Arvin, M., Tahernezhad, P., 2019. Chemical composition, petrology and P-T conditions of Ti-Mg-biotites within syenitic rocks from the Lar igneous suite, east of Iran. Int. J. Geol. Environ. Eng. 13, 524–528.
Ghasemi, H., Sadeghian, M., Kord, M., Khanalizadeh, A., 2010. The evolution mechanisms of Zahedan granitoid batholith, Southeast Iran. Iran. J. Crystallogr. Mineral. 17, 551–578.
Golonka, J., 2004. Plate tectonic evolution of the southern margin of Eurasia in the Mesozoic and Cenozoic. Tectonophysics 381, 235–273. https://doi.org/10.1016/j.tecto.2002.06.004.
Gülmez, F., Prelević, D., Förster, M.W., Buhre, S., Günther, J., 2023. Experimental production of K-rich metasomes through sediment recycling at the slab-mantle interface in the fore-arc. Sci. Rep. 13, 19608. https://doi.org/10.1038/s41598-023-46367-7.
Hart, S.R., 1984. A large-scale isotope anomaly in the Southern Hemisphere mantle. Nature 309, 753–757. https://doi.org/10.1038/309753a0.
Hermann, J., Green, D.H., 2001. Experimental constraints on high pressure melting in subducted crust. Earth Planet. Sci. Lett. 188, 149–168. https://doi.org/10.1016/S0012-821X(01)00321-1.
Hofmann, A.W., 1997. Mantle geochemistry: the message from oceanic volcanism. Nature 385, 219–229. https://doi.org/10.1038/385219a0.
Ionov, D.A., Hofmann, A.W., 1995. Nb-Ta-rich mantle amphiboles and micas: implications for subduction-related metasomatic trace element fractionations. Earth Planet. Sci. Lett. 131, 341–356. https://doi.org/10.1016/0012-821X(95)00037-D.
Iwano, H., Orihashi, Y., Hirata, T., Ogasawara, M., Danhara, T., Horie, K., Hasebe, N., Sueoka, S., Tamura, A., Hayasaka, Y., 2013. An inter-laboratory evaluation of OD-3 zircon for use as a secondary U–Pb dating standard. Island Arc 22, 382–394. https://doi.org/10.1111/iar.12038.
Jentzer, M., Agard, P., Bonnet, G., Monié, P., Fournier, M., Whitechurch, H., Omrani, J., Zarrinkoub, M.H., Khatib, M.M., Kohansal, R., Do Couto, D., Godbillot, C., Ninkabou, D., 2022. The North Sistan orogen (Eastern Iran): tectono-metamorphic evolution and significance within the Tethyan realm. Gondwana Res. 109, 460–492. https://doi.org/10.1016/j.gr.2022.04.004.
Jung, D., Keller, J., Khorasani, R., Marcks, C., Baumann, A., Horn, P., 1984. Petrology of the Tertiary magmatic activity in the northern Lut area east Iran, 160. Neues Jahrbuch fur Geologie und Palaontologie Abhandlungen, pp. 417–467.
Kessel, R., Ulmer, P., Pettke, T., Schmidt, M.W., Thompson, A.B., 2005. The water–basalt system at 4 to 6 GPa: phase relations and second critical endpoint in a K-free eclogite at 700 to 1400°C. Earth Planet. Sci. Lett. 237, 873–892. https://doi.org/10.1016/j.epsl.2005.06.018.
Kirkland, C.L., Smithies, R.H., Taylor, R.J.M., Evans, N., McDonald, B., 2015. Zircon Th/U ratios in magmatic environs. Lithos 212–215, 397–414. https://doi.org/10.1016/j.lithos.2014.11.021.
Kurzawa, T., Bröcker, M., Rad, G.F., Berndt, J., Lisker, F., 2017. Cretaceous high-pressure metamorphism and low pressure overprint in the Sistan Suture Zone, eastern Iran: additional temperature estimates for eclogites, geological significance of U-Pb zircon ages and Rb-Sr constraints on the timing of exhumation. J. Asian Earth Sci. 147, 332–344. https://doi.org/10.1016/j.jseaes.2017.07.051.
LaTourrette, T., Hervig, R.L., Holloway, J.R., 1995. Trace element partitioning between amphibole, phlogopite, and basanite melt. Earth Planet. Sci. Lett. 135, 13–30. https://doi.org/10.1016/0012-821X(95)00146-4.
Le Maitre, R.W., 2002. A Classification of Igneous Rocks and Glossary of Terms. Cambridge University Press, Cambridge.
Ludwig, K.R., 2012. User's manual for Isoplot version 3.75–4.15: a geochronological tool kit for Microsoft Excel. Berkeley Geochronological Center Special Publication 5.
McCall, G.J.H., 1997. The geotectonic history of the Makran and adjacent areas of southern Iran. J. Asian Earth Sci. 15, 517–531. https://doi.org/10.1016/S0743-9547(97)00032-9.
McDonough, W.F., 1990. Constraints on the composition of the continental lithospheric mantle. Earth Planet. Sci. Lett. 101, 1–18. https://doi.org/10.1016/0012-821X(90)90119-I.
Moghadam, H.S., Zaki Khedr, M., Chiaradia, M., Stern, R.J., Bakhshizad, F., Arai, S., Ottley, C.J., Tamura, A., 2014. Supra-subduction zone magmatism of the Neyriz ophiolite, Iran: constraints from geochemistry and Sr-Nd-Pb isotopes. Int. Geol. Rev. 56, 1395–1412. https://doi.org/10.1080/00206814.2014.942391.
Mohammadi, A., Burg, J.P., Bouilhol, P., Ruh, J., 2016. U-Pb geochronology and geochemistry of Zahedan and Shah Kuh plutons, Southeast Iran: implication for closure of the South Sistan suture zone. Lithos 248-251, 293–308. https://doi.org/10.1016/j.lithos.2016.02.003.
Mohammadi, A., Burg, J.P., Ruh, J.B., Spezzaferri, S., 2023. Clastic carbonates in the South Sistan Basin (SE Iran): implications for subduction vergence and timing of collision. Int. Geol. Rev. 65, 3453–3465. https://doi.org/10.1080/00206814.2023.2191119.
Moradi, R., Boomeri, M., Bagheri, S., 2014. Petrography and geochemistry of intrusive rocks in the Shurchah antimony-bearing area Southeast of Zahedan. Petrol. J. (Isfahan Univ.) 5, 15–32.
Moradi, R., Boomeri, M., Bagheri, S., Nakashima, K., 2016. Mineral chemistry of igneous rocks in the lar Cu-Mo prospect, southeastern part of Iran: implications for P, T, and fO2. Turk. J. Earth Sci. 25, 418–433. https://doi.org/10.3906/yer-1510-5.
Nadermezerji, S., Karimpour, M.H., Shafaroudi, A.M., Santos, J.F., Mathur, R., Ribeiro, S., 2018. U-Pb geochronology, Sr–Nd isotopic compositions, geochemistry and petrogenesis of Shah Soltan Ali granitoids, Birjand Eastern Iran. Geochemistry 78, 299–313. https://doi.org/10.1016/j.chemer.2018.08.003.
Natali, C., Aghazadeh, M., Braschi, E., Avanzinelli, R., Badrzadeh, Z., Bianchini, G., Casalini, M., Agostini, S., Mattei, M., Conticelli, S., 2024. Ages, geochemistry and Sr-Nd-Pb isotopes of alkaline potassic volcanic rocks from the Ahar-Arasbaran region (NW Iran): evidence for progressive evolution of mantle sources during the Neotethyan subduction system. Lithos 470-471, 107504. https://doi.org/10.1016/j.lithos.2024.107504.
Omidianfar, S., Monsef, I., Rahgoshay, M., Zheng, J., Cousens, B., 2020. The middle Eocene high-K magmatism in Eastern Iran Magmatic Belt: constraints from U-Pb zircon geochronology and Sr-Nd isotopic ratios. Int. Geol. Rev. 62, 1751–1768. https://doi.org/10.1080/00206814.2020.1716272.
Omidianfar, S., Monsef, I., Rahgoshay, M., Moghadam, H.S., Cousens, B., Chen, M., Rajabpour, S., Zheng, J., 2023. Neo-Tethyan subduction triggered Eocene–Oligocene magmatism in eastern Iran. Geol. Mag. 160, 490–510. https://doi.org/10.1017/S0016756822001066.
Pang, K.-N., Chung, S.-L., Zarrinkoub, M.H., Khatib, M.M., Mohammadi, S.S., Chiu, H.-Y., Chu, C.-H., Lee, H.-Y., 2013. Eocene-Oligocene post-collisional magmatism in the Lut-Sistan region, eastern Iran: magma genesis and tectonic implications. Lithos 180-181, 234–251. https://doi.org/10.1016/j.lithos.2013.05.009.
Paton, C., Hellstrom, J., Paul, B., Woodhead, J., Hergt, J., 2011. Iolite: freeware for the visualisation and processing of mass spectrometric data. J. Anal. At. Spectrom. 26, 2508–2518. https://doi.org/10.1039/C1JA10172B.
Peccerillo, A., Taylor, S., 1976. Geochemistry of Eocene calc-alkaline volcanic rocks from the Kastamonu area, northern Turkey. Contrib. Mineral. Petrol. 58, 63–81. https://doi.org/10.1007/BF00384745.
Petrus, J.A., Kamber, B.S., 2012. VizualAge: a novel approach to laser ablation ICP-MS U-Pb geochronology data reduction. Geostand. Geoanal. Res. 36, 247–270. https://doi.org/10.1111/j.1751-908X.2012.00158.x.
Prelević, D., Akal, C., Foley, S.F., Romer, R., Conticelli, S., 2008. Mediterranean tertiary lamproites derived from multiple source components in postcollisional geodynamics. Geochim. Cosmochim. Acta 72, 2125–2156. https://doi.org/10.1016/j.gca.2008.01.029.
Rabiee, A., Rossetti, F., Lucci, F., Lustrino, M., 2022. Cenozoic porphyry and other hydrothermal ore deposits along the South Caucasus-West Iranian tectono-magmatic belt: a critical reappraisal of the controlling factors. Lithos 430-431, 106874. https://doi.org/10.1016/j.lithos.2022.106874.
Rabiee, A., Rossetti, F., Lustrino, M., Azizi, H., Asahara, Y., Alipour, S., Selby, D., 2024. Formation and degradation of a porphyry occurrence: the Oligocene Khatoon-Abad porphyry Mo-Cu system, NW Iran. Ore Geol. Rev. 174, 106330. https://doi.org/10.1016/j.oregeorev.2024.106330.
Rapp, R.P., Shimizu, N., Norman, M.D., Applegate, G.S., 1999. Reaction between slab-derived melts and peridotite in the mantle wedge: experimental constraints at 3.8 GPa. Chem. Geol. 160, 335–356. https://doi.org/10.1016/S0009-2541(99)00106-0.
Richards, J.P., Spell, T., Rameh, E., Razique, A., Fletcher, T., 2012. High Sr/Y magmas reflect arc maturity, high magmatic water content, and porphyry Cu ± Mo ± Au potential: examples from the Tethyan Arcs of Central and Eastern Iran and Western Pakistan. Econ. Geol. 107, 295–332. https://doi.org/10.2113/econgeo.107.2.295.
Rossetti, F., Monié, P., Nasrabady, M., Theye, T., Lucci, F., Saadat, M., 2017. Early Carboniferous subduction-zone metamorphism preserved within the Palaeo-Tethyan Rasht ophiolites (western Alborz, Iran). J. Geol. Soc. Lond. 174, 741–758. https://doi.org/10.1144/jgs2016-130.
Rubatto, D., Muentener, O., Barnhoorn, A., Gregory, C., 2008. Zircon: the metamorphic mineral. Am. Mineral. 93, 1519–1529. https://doi.org/10.2138/rmg.2017.83.9.
Saadat, S., Stern, C.R., 2012. Petrochemistry of a xenolith-bearing Neogene alkali olivine basalt from northeastern Iran. J. Volcanol. Geotherm. Res. 225-226, 13–29. https://doi.org/10.1016/j.jvolgeores.2012.02.014.
Saccani, E., Delavari, M., Beccaluva, L., Amini, S., 2010. Petrological and geochemical constraints on the origin of the Nehbandan ophiolitic complex (eastern Iran): implication for the evolution of the Sistan Ocean. Lithos 117, 209–228. https://doi.org/10.1016/j.lithos.2010.02.016.
Saccani, E., Allahyari, K., Beccaluva, L., Bianchini, G., 2013. Geochemistry and petrology of the Kermanshah ophiolites (Iran): implication for the interaction between passive rifting, oceanic accretion, and OIB-type components in the Southern Neo-Tethys Ocean. Gondwana Res. 24, 392–411. https://doi.org/10.1016/j.gr.2012.10.009.
Sadeghian, M., Valizadeh, M.V., 2007. Emplacement mechanism of Zahedan granitoidic pluton with the aid of AMS method. Earth Sci. 17, 126–143. https://doi.org/10.22071/gsj.2008.57653.
Samiee, S., Karimpour, M.H., Ghaderi, M., Haidarian Shahri, M.R., Kloetzli, O., Santos, J.F., 2016. Petrogenesis of sub-volcanic rocks from the Khunik prospecting area, south of Birjand, Iran: geochemical, Sr–Nd isotopic and U–Pb zircon constraints. J. Asian Earth Sci. 115, 170–182. https://doi.org/10.1016/j.jseaes.2015.09.023.
Sargazi, M., Bagheri, S., Ma, X., 2022. Oligocene calc-alkaline lamprophyres and K-rich association in the eastern Iranian ranges: products of low-degree melting of subduction-modified lithospheric mantle in post-orogenic setting. Lithos 430-431, 106864. https://doi.org/10.1016/j.lithos.2022.106864.
Schmidt, M.W., Poli, S., 1998. Experimentally based water budgets for dehydrating slabs and consequences for arc magma generation. Earth Planet. Sci. Lett. 163, 361–379. https://doi.org/10.1016/S0012-821X(98)00142-3.
Schmidt, M.W., Vielzeuf, D., Auzanneau, E., 2004. Melting and dissolution of subducting crust at high pressures: the key role of white mica. Earth Planet. Sci. Lett. 228, 65–84. https://doi.org/10.1016/j.epsl.2004.09.020.
Schoene, B., Bowring, S.A., 2006. U–Pb systematics of the McClure Mountain syenite: thermochronological constraints on the age of the 40Ar/39Ar standard MMhb. Contrib. Mineral. Petrol. 151, 615–630. https://doi.org/10.1007/s00410-006-0077-4.
Sepidbar, F., Mirnejad, H., Ma, C., Moghadam, H.S., 2018. Identification of Eocene-Oligocene magmatic pulses associated with flare-up in East Iran: timing and sources. Gondwana Res. 57, 141–156. https://doi.org/10.1016/j.gr.2018.01.008.

Skora, S., Blundy, J.D., Brooker, R.A., Green, E.C., de Hoog, J., Connolly, J.A., 2015. Hydrous phase relations and trace element partitioning behaviour in calcareous sediments at subduction-zone conditions. J. Petrol. 56, 953–980. https://doi.org/10.1093/petrology/egv024.

Sláma, J., Košler, J., Condon, D.J., Crowley, J.L., Gerdes, A., Hanchar, J.M., Horstwood, M.S.A., Morris, G.A., Nasdala, L., Norberg, N., Schaltegger, U., Schoene, B., Tubrett, M.N., Whitehouse, M.J., 2008. Plešovice zircon — a new natural reference material for U–Pb and Hf isotopic microanalysis. Chem. Geol. 249, 1–35. https://doi.org/10.1016/j.chemgeo.2007.11.005.

Stampfli, G.M., Hochard, C., Vérard, C., Wilhem, C., vonRaumer, J., 2013. The formation of Pangea. Tectonophysics 593, 1–19. https://doi.org/10.1016/j.tecto.2013.02.037.

Sun, S.-S., McDonough, W.F., 1989. Chemical and isotopic systematics of oceanic basalts: implications for mantle composition and processes. Geol. Soc. Lond. Spec. Publ. 42, 313–345. https://doi.org/10.1144/GSL.SP.1989.042.01.19.

Tirrul, R., Bell, I., Griffis, R., Camp, V., 1983. The Sistan suture zone of eastern Iran. Geol. Soc. Am. Bull. 94, 134–150. https://doi.org/10.1130/0016-7606(1983)94<134:TSSZOE>2.0.CO;2.

Tommasini, S., Avanzinelli, R., Conticelli, S., 2011. The Thorium/Lanthanum conundrum of the Tethyan realm lamproites: the role of recycled sediments and zoisite/lawsonite melting. Earth Planet. Sci. Lett. 301, 469–478. https://doi.org/10.1016/j.epsl.2010.11.023.

Verdel, C., Wernicke, B.P., Hassanzadeh, J., Guest, B., 2011. A Paleogene extensional arc flare-up in Iran. Tectonics 30, TC3008. https://doi.org/10.1029/2010TC002809.

Vermeesch, P., 2018. IsoplotR: a free and open toolbox for geochronology. Geosci. Front. 9, 1479–1493. https://doi.org/10.1016/j.gsf.2018.04.001.

Visonà, D., Nimis, P., Cavazzini, G., Fioretti, A.M., Laurenzi, M.A., Massironi, M., Villa, I. M., 2025. Alkaline magmatism in the post-orogenic Triassic Predazzo complex, Dolomites, NE Italy: ages and significance. Lithos 494–495, 107912. https://doi.org/10.1016/j.lithos.2024.107912.

Weis, D., Kieffer, B., Maerschalk, C., Barling, J., de Jong, J., Williams, G.A., Hanano, D., Pretorius, W., Mattielli, N., Scoates, J.S., Goolaerts, A., Friedman, R.M., Mahoney, J. B., 2006. High-precision isotopic characterization of USGS reference materials by TIMS and MC-ICP-MS. Geochem. Geophys. Geosyst. 7, Q08006. https://doi.org/10.1029/2006GC001283.

Whitney, D.L., Evans, B.W., 2010. Abbreviations for names of rock-forming minerals. Am. Mineral. 95, 185–187. https://doi.org/10.2138/am.2010.3371.

Wiedenbeck, M., Alle, P., Corfu, F., Griffin, W., Meier, M., Oberli, v., F., Quadt, v., A., Roddick, J., Spiegel, W., 1995. Three natural zircon standards for U-Th-Pb, Lu-Hf, trace element and REE analyses. Geostand. Newslett. 19, 1–23. https://doi.org/10.1111/j.1751-908X.1995.tb00147.x.

Woolley, A.R., Bergman, S.C., Edgar, A.D., Le Bas, M.J., Mitchell, R.H., Rock, N.M.S., Scott-Smith, B.H., 1996. Classification of lamprophyres, lamproites, kimberlites, and the kalsilitic, melilitic, and leucitic rocks. Can. Mineral. 34, 175–186.

Zanchi, A., Berra, F., Mattei, M., Ghassemi, M.R., Sabouri, J., 2006. Inversion tectonics in central Alborz, Iran. J. Struct. Geol. 28, 2023–2037. https://doi.org/10.1016/j.jsg.2006.06.020.

Zanchi, A., Zanchetta, S., Berra, F., Mattei, M., Garzanti, E., Molyneux, S., Nawab, A., Sabouri, J., 2009. The Eo-Cimmerian (late? Triassic) orogeny in North Iran. Geol. Soc. Lond. Spec. Publ. 312, 31–55. https://doi.org/10.1144/SP312.3.

Zarrinkoub, M.H., Pang, K.-N., Chung, S.-L., Khatib, M.M., Mohammadi, S.S., Chiu, H.-Y., Lee, H.-Y., 2012. Zircon U–Pb age and geochemical constraints on the origin of the Birjand ophiolite, Sistan suture zone, eastern Iran. Lithos 154, 392–405. https://doi.org/10.1016/j.lithos.2012.08.007.

Zindler, A., Hart, S., 1986. Chemical geodynamics. Annu. Rev. Earth Planet. Sci. 14, 493–571. https://doi.org/10.1146/annurev.ea.14.050186.002425.